1   # A structural mechanism for phosphorylation-dependent inactivation of the
2   # AP2 complex

3   Edward A. Partlow[1],*, Richard W. Baker[2],*,#, Gwendolyn M. Beacham[1], Joshua S. Chappie[1],
4   Andres E. Leschziner[2,3],#, Gunther Hollopeter[1],#

5   **Affiliations**
6   1. Department of Molecular Medicine, Cornell University, Ithaca, New York, USA.
7   2. Department of Cellular & Molecular Medicine, School of Medicine, University of California
8   San Diego, La Jolla, California 92093, USA.
9   3. Section of Molecular Biology, Division of Biological Sciences, University of California San
10 Diego, La Jolla, California 92093, USA.
11 * These authors contributed equally to this work.
12 # Correspondence to: ribaker@ucsd.edu (R.W.B.); aleschziner@ucsd.edu (A.E.L.);
13 gh383@cornell.edu (G.H.).
14

15 **Abstract**

16 Endocytosis of transmembrane proteins is orchestrated by the AP2 clathrin adaptor

17 complex. AP2 dwells in a closed, inactive state in the cytosol, but adopts an open, active

18 conformation on the plasma membrane. Membrane-activated complexes are also phosphorylated,

19 but the significance of this mark is debated. We recently proposed that NECAP negatively

20 regulates AP2 by binding open and phosphorylated complexes (Beacham *et al.*, 2018). Here, we

21 report high-resolution cryo-EM structures of NECAP bound to phosphorylated AP2. The site of

22 AP2 phosphorylation is directly coordinated by residues of the NECAP PHear domain that are

23 predicted from genetic screens in *C. elegans*. Using membrane mimetics to generate

24 conformationally open AP2, we find that a second domain of NECAP binds these complexes and

25 cryo-EM reveals both domains of NECAP engaging closed, inactive AP2. Assays *in vitro* and *in*

26 *vivo* confirm these domains cooperate to inactivate AP2. We propose that phosphorylation marks

27 adaptors for inactivation.

28   **Introduction**

29   Clathrin-Mediated Endocytosis (CME) enables cells to dynamically regulate the

30   composition of the plasma membrane and mediate uptake of transmembrane cargo, such as

31   ligand-bound receptors. This process is orchestrated by the clathrin Adaptor Protein 2 complex

32   (AP2), which interacts with much of the endocytic machinery and functions during the earliest

33   stages of CME (Mettlen et al., 2018). Inactive, closed AP2 is initially recruited to the cytosolic

34   face of the plasma membrane through its interaction with PhosphatidylInositol-4,5-bisPhosphate

35   (PIP_2) (Collins et al., 2002; Höning et al., 2005). At the plasma membrane, conformational

36   rearrangement of AP2 to an active, open conformation is promoted by membrane-associated

37   muniscin proteins (Henne et al., 2010; Hollopeter et al., 2014; Umasankar et al., 2014) (Figure

38   1A). Conversion of AP2 to the open conformation exposes a second binding site for PIP_2 that

39   stabilizes membrane engagement (Kadlecova et al., 2017), and also reveals binding sites for

40   clathrin and membrane-embedded cargo (Jackson et al., 2010; Kelly et al., 2014). These

41   interactions allow AP2 to function as the central regulatory hub of clathrin-coated vesicle

42   formation (Kirchhausen et al., 2014).

43   After opening, AP2 is phosphorylated on the mu subunit (Conner et al., 2003; Jackson et

44   al., 2003; Pauloin et al., 1982), but the role of this mark remains poorly defined, in part because

45   no structures have yet visualized the phosphorylated threonine. Some data suggest that

46   phosphorylation of AP2 enhances binding to PIP_2 and cargo (Fingerhut et al., 2001; Höning et

47   al., 2005; Ricotta et al., 2002). Additionally, mutation of the phosphorylated threonine (mu

48   T156A) or addition of kinase inhibitors have been shown to inhibit transferrin uptake in tissue

49   culture (Olusanya et al., 2001), implying that phosphorylation promotes AP2 activity. Two

50   kinases have been shown to phosphorylate AP2 (mu T156) *in vitro*: AP2-Associated Kinase

51   (AAK1) (Conner and Schmid, 2002) and cyclin-G associated kinase (GAK) (Umeda et al.,

52   2000). Curiously, studies involving these kinases suggest that phosphorylation may function in

53   an inactivation pathway, as AAK1 appears to inhibit endocytosis using *in vitro* assays (Conner

54   and Schmid, 2002), and GAK seems to function in vesicle uncoating (Taylor et al., 2011).

55   Whether phosphorylation is an activating or inactivating mark, and whether it functions in

56   multiple stages in the endocytic pathway remains to be determined.

57   While the pathways of clathrin adaptor activation have been well characterized both

58   structurally and biochemically (Collins et al., 2002; Kelly et al., 2008, 2014; Jackson et al., 2010;

59   Ren et al., 2013; Jia et al., 2014), it is unknown whether inactivation of AP2 is also a regulated

60   process. Adaptor inactivation likely occurs throughout the endocytic cycle. High-resolution

61   imaging reveals that many endocytic pits abort prematurely, presumably when a requirement for

62   activation is unmet, such as an absence of PIP_2, cargo, or muniscin (Cocucci et al., 2012;

63   Kadlecova et al., 2017). Abortive events could represent a mechanism to limit futile vesicle

64   formation in the absence of cargo or prevent ectopic budding from off-target membranes lacking

65   PIP_2. Additionally, when adaptors are removed from vesicles prior to fusion with target

66   organelles, they must also revert to the cytosolic, inactive state. Adaptor uncoating appears to

67   require PIP_2 phosphatase activity (Cremona et al., 1999; He et al., 2017), but it is not known

68   whether PIP_2 hydrolysis is sufficient to uncoat AP2, as cytosol and ATP are required *in vitro*

69   (Hannan et al., 1998). It remains to be determined whether adaptor inactivation occurs via

70   stochastic disassembly of endocytic pits (Ehrlich et al., 2004), or if it is driven by regulated

71   mechanisms, such as an endocytic checkpoint to ensure cargo incorporation (Loerke et al., 2009;

72   Puthenveedu and von Zastrow, 2006).

73   We recently found that NECAP appears to act as a negative regulator of AP2 *in vivo*

74   (Beacham *et al.*, 2018). NECAP is a coat-associated protein that binds to the alpha appendage

75   and beta linker regions of AP2 to facilitate endocytic accessory protein recruitment to sites of

76   endocytosis (Ritter et al., 2003, 2004, 2007, 2013). In *C. elegans*, loss of the muniscin, *fcho-1*,

77   causes AP2 to dwell in an inactive, closed state (Hollopeter *et al.*, 2014). Deletion of the gene

78   encoding NECAP (*ncap-1*) in *fcho-1* mutants restores AP2 to an active, open and phosphorylated

79   state, suggesting that NECAP counterbalances AP2 activation. Consistent with this model,

80   NECAP binds open and phosphorylated AP2 complexes *in vitro*, however it is unclear how

81   NECAP recognizes the open and phosphorylated states and whether NECAP can directly close

82   these complexes.

83   Here, we determined cryo-EM structures of NECAP-AP2 complexes which show that

84   NECAP clamps AP2 complexes into the closed, inactive conformation. This mechanism requires

85   coincident binding of two domains of NECAP, one of which confers specificity for open

86   complexes, and another that detects AP2 phosphorylation. Our structures are supported by *in*

87   *vitro* biochemistry along with functional assays and unbiased genetic screens in *C. elegans*.

88   Importantly, the site of AP2 phosphorylation is directly bound by NECAP, defining

89   phosphorylation as a key step in the dynamic regulation of AP2 inactivation.

90

91   **Results**

92   **Structural basis for recognition of phosphorylated AP2 by NECAP**

93   We previously demonstrated that NECAP binds to the phosphorylated AP2 core

94   (Beacham et al., 2018). NECAP is a ~29 kDa, soluble protein composed of three domains: an N-

95   terminal P̲leckstrin H̲omology with e̲a̲r̲-like function (NECAP$_{PHear}$), a central E̲xtended region of

96   conservation (NECAP$_{Ex}$), and a C-terminal domain with low conservation (NECAP$_{Tail}$) (Figure

97   1B) (Ritter et al., 2007, 2013). To narrow down which domain of NECAP binds phosphorylated

98   AP2, we performed *in vitro* pulldown assays using NECAP truncations and phosphorylated AP2

99   cores lacking appendages (phosphoAP2; rodent; boxed in Figure 1A). Our analysis showed that

100   NECAP$_{PHear}$ is necessary and sufficient to bind phosphorylated AP2 *in vitro* (Figure 1C).

101   Phosphorylation is thought to stabilize the open conformation of AP2 and we previously

102   showed that NECAP can bind open AP2 that is not phosphorylated. To understand whether

103   NECAP binds to the site of phosphorylation or a conformation induced by phosphorylation, we

104   determined a ~3.2 Å cryo-EM structure of the phosphorylated AP2 core bound to full-length

105   NECAP2 (mouse; Figure 1D, Figure 1—figure supplement 1, Figure 1—figure supplement 2,

106   Table 1). Globally, AP2 has adopted a conformation similar to the crystal structure of the closed

107   complex (PDB 2VGL; Figure 1—figure supplement 2A) (Collins et al., 2002), which is inactive

108   due to the occlusion of binding sites for cargo and the plasma membrane. We observe density for

109   the entire AP2 core, with additional density contacting the mu subunit (Figure 1—figure

110   supplement 2A). Most of this additional density can be attributed to NECAP$_{PHear}$, due to

111   similarity with a solution NMR structure of the mouse NECAP1 PHear domain (PDB 1TQZ;

112   Figure 1—figure supplement 2B, C) (Ritter et al., 2007). The remaining unassigned density at

113   this interface extends from the amino terminus of residue 159 of mu, and can be attributed to the

114   phosphorylated mu linker (amino acids 154-158, Figure 1—figure supplement 2C). Our structure

115   is of sufficient quality to build a near-complete molecular model for the phosphoAP2-NECAP

116   complex, which shows that residues in NECAP$_{PHear}$ interact directly with the phosphorylated mu

117   T156 (pT156; see Figure 3B below). These data show that the phosphorylated complex can exist

118   in a closed conformation and suggest that the mechanism of NECAP binding to open complexes

119   that are not phosphorylated must be fundamentally different.

120

121   **A genetic screen in *C. elegans* identifies mutations that disrupt the NECAP-AP2 interface**

122   Our structural data using vertebrate proteins imply that NECAP$_{PHear}$ and its interaction

123   with mu pT156 is central to the function of NECAP. To test this hypothesis, we turned to *C.*

124   *elegans*, where we devised a genetic strategy to specifically isolate critical residues required for

125   NECAP interaction with AP2, while avoiding mutations that destabilize the NECAP protein

126   (Figure 2A). This screen was based on our previous screen for mutations that suppressed the

127   morphological and fitness defects of *fcho-1* mutants and restored the active, open state of AP2.

128   In the original screen, the predominant mutations identified were either gain-of-function

129   mutations in AP2 subunits that destabilize the closed conformation (Hollopeter et al., 2014) or

130   null mutations in the gene encoding NECAP, *ncap-1* (Beacham et al., 2018). To identify rare

131   mutations that specifically disrupt the functional interface between AP2 and NECAP, we

132   repeated the screen with a fluorescent tag on NECAP to enable secondary classification of

133   suppressed animals based on fluorescent hallmarks (Figure 2A). Because gain of function

134   mutations in AP2 result in NECAP recruitment to the nerve ring, a membranous tissue with a

135   high concentration of AP2 (Beacham et al., 2018), we visually eliminated suppressed animals

136   that had fluorescent nerve rings. We also eliminated suppressed animals that were no longer

137   fluorescent, as these likely harbored null mutations in NECAP. We reasoned that the remaining

138   animals, which suppressed *fcho-1* phenotypes without altering the fluorescent signal, might

139   possess missense mutations that prevented NECAP from binding AP2. Worms that met these

140   requirements were selected, and the genes encoding NECAP and AP2 were sequenced. We

141   isolated mutations in NECAP$_{PHear}$ and AP2 mu that were previously proposed to disrupt

142   NECAP-AP2 interaction, as well as new potential interface mutations in the AP2 alpha and beta

143   subunits (Figure 2B and 2C). Strikingly, the overwhelming majority of mutations (8 out of 13)

144   isolated were in mu T156, suggesting that phosphorylation of this residue generates the substrate

145   for NECAP activity.

146

147   **Coordination of phosphorylated AP2 by NECAP is required for inactivation**

148   To understand how the mutated residues isolated in our screens disrupt NECAP function,

149   we mapped the vertebrate equivalents onto our cryo-EM structure (Figure 3A, B). Mutations of

150   T156 itself disable phosphorylation completely, and the two residues in NECAP$_{PHear}$ (A32 and

151   S87) lie within 10 Å of mu T156, which suggests that they disrupt coordination of the phosphate

152   group and explains how they might break the AP2-NECAP interaction *in vivo* (throughout the

153   text, all residue numbers are for vertebrate proteins, see Figure 2C for *C. elegans* equivalents).

154   We also noticed that NECAP R112 forms electrostatic interactions with the T156

155   phosphorylation mark and may be required for binding (Figure 3B). To test the hypothesis that

156   coordination of mu T156 phosphorylation is necessary for NECAP function, we introduced these

157   mutations into recombinant vertebrate complexes and *C. elegans* strains and tested each using a

158   panel of *in vitro* and *in vivo* assays.

159   As predicted, mutation of NECAP R112 disrupted binding *in vitro*, similar to either

160   mutations in the mu linker (T156A) or NECAP$_{PHear}$ (S87N) (Figure 3C). Consistent with the

161   screen, the mutations suppressed the morphological and fitness defects of *fcho-1* mutants, as

162   quantified by the number of days for a population to expand and consume a food source (Figure

163   3D). Furthermore, all three mutations reduced NECAP recruitment to the *C. elegans* nerve ring

164   (Figure 3E) and resulted in accumulation of open AP2 complexes according to an *in vivo*

165   protease sensitivity assay (Figure 3F). Together, our data show that NECAP$_{PHear}$ binding to the

166   phosphorylated threonine dictates AP2 inactivation.

167   While the AP2-NECAP$_{PHear}$ interface is clearly important for inactivation, our cryo-EM

168   structure does not explain why. NECAP$_{PHear}$ only contacts the mu subunit of AP2, and there are

169   no clashes when mu-NECAP$_{PHear}$ is modeled as a rigid body into the crystal structure of open

170   AP2 (PDB 2XA7; Figure 3—figure supplement 1). Additionally, NECAP$_{PHear}$ does not block

171   cargo- or PIP$_2$-binding sites and no obvious steric clashes would prevent AP2 from transitioning

172   between open and closed states when bound to NECAP$_{PHear}$ (Figure 3—figure supplement 1).

173   One feature that might prevent NECAP$_{PHear}$ binding to the open conformation is that mu T156 is

174   packed against the beta subunit of AP2 in this structure (Figure 3—figure supplement 1C)

175   (Jackson et al., 2010). This suggests that release and phosphorylation of the mu linker are

176   important regulatory steps in NECAP recruitment. Nonetheless, while NECAP$_{PHear}$ is required to

177   inactivate AP2, binding of NECAP$_{PHear}$ alone does not explain inactivation. Because mutations in

178   NECAP$_{PHear}$ do not disrupt binding to open, non-phosphorylated AP2 complexes (Beacham et

179   al., 2018), we believe another domain of NECAP may contribute to its function.

180

181   **Membrane mimetics stimulate opening of AP2**

182   To understand how NECAP recognizes open AP2 in the absence of phosphorylation, we

183   needed to control and measure the conformation of AP2 *in vitro*. We used structural data to

184   engineer a protease site on AP2 that is preferentially cleaved in the open state (Aguilar et al.,

185   1997; Hollopeter et al., 2014; Matsui and Kirchhausen, 1990) (Figure 4A) and introduced a

186   mutation in the mu subunit (mu E302K) that is known to promote the open conformation

187 (Hollopeter et al., 2014). Despite this mutation, our AP2 complexes remained largely protease

188 insensitive (i.e. closed) in the absence of other factors (Figure 4B). To produce open AP2, we

189 turned to the observation that binding of AP2 to cargo is dramatically stimulated by the addition

190 of long chain heparin (Jackson et al., 2010). Long anionic polymers are hypothesized to mimic

191 negatively-charged PIP_2-containing membranes. To test whether these types of negatively

192 charged macromolecules could affect AP2 conformation, we included them in our protease

193 sensitivity assay. Indeed, two anionic polymers, heparin and nucleic acids, generated protease-

194 sensitive complexes, suggesting that they stimulated a conformational rearrangement of AP2 to

195 the open state (Figure 4B). Importantly, the PIP_2 mimetic, inositol hexakisphosphate (IP6),

196 blocks the stimulatory effect of DNA on AP2, suggesting that polymers engage known PIP_2

197 binding sites (Figure 4B).

198   We confirmed that our protease-sensitivity assay was reporting structural changes using

199 2D classification of AP2 cryo-EM images. In the absence of a DNA oligo, both mu E302K and

200 wild-type AP2 adopted a conformation that matches the crystal structure of the closed complex

201 (PDB 2VGL; Figures 4C-4E). In the presence of an anionic membrane mimetic (47 nucleotide

202 DNA), ~60% of wild type and more than 90% of AP2 (mu E302K) particles were open (Figures

203 4C-4E, Figure 4—figure supplement 1). On the basis of these results we refer to AP2 (mu

204 E302K) in the presence of anionic polymer as 'open AP2' in our experiments. In addition, this

205 cryo-EM data suggests that the membrane itself affects the conformational equilibrium of AP2

206 and demonstrates that we can control the conformation of AP2 *in vitro* using a defined chemical

207 substrate. Using our method to generate open AP2, we confirmed that NECAP bound these

208 complexes in the absence of phosphorylation (Figure 4F).

209

NECAP$_{Ex}$ recognizes membrane-activated AP2

210

211   To identify the domain of NECAP that engages open AP2, we tested NECAP truncations

212   (Figure 1B) and found that NECAP$_{Ex}$ was necessary and sufficient for binding (Figure 5A). This

213   supports previous data that binding of NECAP$_{PHear}$ to AP2 in rat brain lysate is enhanced by the

214   presence of NECAP$_{Ex}$ (Ritter et al., 2013) and explains why NECAP$_{PHear}$ mutants retain this

215   binding (Beacham *et al.*, 2018). Because the open state of AP2 precedes phosphorylation

216   (Conner et al., 2003; Hollopeter et al., 2014), we hypothesize NECAP$_{Ex}$ may form an initial

217   priming interaction with open AP2 prior to phosphorylation.

218   To visualize NECAP bound to an activated, phosphorylated AP2 complex, we

219   determined a ~3.5 Å structure of phosphorylated AP2 (mu E302K) bound to full-length

220   NECAP2 in the presence of an anionic polymer (DNA) (Figures 5B, Figure 5—figure

221   supplement 1, Table 1). In contrast to other AP2 (mu E302K) complexes incubated with DNA,

222   (Figures 4B and 4E), AP2 was not open, but was in a closed, inactive conformation. As in our

223   previous phosphoAP2-NECAP structure, NECAP$_{PHear}$ was bound to the mu subunit, coordinating

224   pT156. However, in this new structure we observed additional density contacting the beta

225   subunit (Figure 5B). Comparing isosurface threshold levels of the unsharpened, refined map

226   clearly shows that this density is contiguous and extends from the C-terminus of NECAP$_{PHear}$

227   (Figure 6—figure supplement 1), suggesting it represents NECAP$_{Ex}$. Because we cannot assign a

228   definitive sequence register to the NECAP$_{Ex}$ density in this structure, we model the most ordered

229   region as a poly-alanine peptide. We believe this structure may represent a post-open, inactive

230   conformation of the AP2 complex, corresponding to phospho-AP2 simultaneously bound by

231   NECAP and partially engaged with the membrane via the PIP$_2$ pocket on the alpha subunit. We

232   refer to this structure as 'clamped' phosphoAP2-NECAP.

233   While $NECAP_{Ex}$ appears to make extensive contact with the beta subunit of AP2 in this

234   structure, the differences in AP2 conformation that might account for the appearance of the

235    $NECAP_{Ex}$ binding site are subtle (relative to that lacking DNA, Figure 1D, which we refer to as

236   'unclamped' phosphoAP2-NECAP). The region with the greatest structural changes is the alpha-

237   beta interface, with several helices in the C-terminus of alpha shifting ~1-3 Å (Figure 5—figure

238   supplement 2). Additionally, an alpha helix in beta that is part of the Ex domain binding site

239   appears to partially melt when the Ex domain is bound (Figure 5—figure supplement 2B).

240   Ordered density for DNA is not seen at any of the known PIP_2 binding sites, consistent with

241   observations that PIP_2 binding sites are not ordered pockets but rather a collection of basic

242   residues that protrude into the solvent (Owen et al., 2004). Notably, phosphoAP2-NECAP binds

243   to the single-stranded DNA construct used in this experiment with an affinity of ~60 nM (Figure

244   4—figure supplement 1), suggesting that our sample is > 95% bound to DNA at the

245   concentrations used to make cryo-EM grids (3 μM protein, 15 μM DNA). Importantly, only the

246   PIP_2 binding site on the alpha N-terminus is solvent-exposed in the clamped conformation, so the

247   structural consequences of membrane engagement are fundamentally different in the open

248   (several exposed membrane binding sites) versus the closed (a single membrane binding site)

249   conformations.

250   After our cryo-EM structure revealed the $NECAP_{Ex}$ binding site, we sought to understand

251   the functional consequences of this interaction. Intriguingly, our genetic screen provided an

252   unexpected insight, as it identified two mutations in the AP2 alpha and beta subunits that escape

253   inactivation by NECAP and are in close proximity to the $NECAP_{Ex}$ binding site (Figure 2, Figure

254   6A). Purified AP2 complexes with these mutations have reduced affinity for NECAP *in vitro*

255   (Figure 6B). Additionally, mutation of the most conserved residues of the $NECAP_{Ex}$ domain

256   results in loss of binding to open AP2 (Figure 6B) (Ritter et al., 2013). All three of these

257   mutations recapitulate the NECAP knockout phenotype in our *in vivo* fitness assay (Figure 6C),

258   imaging assay (Figure 6D), and protease sensitivity assay (Figure 6E). These data support the

259   conclusion that $NECAP_{Ex}$ specifically recognizes membrane-activated AP2.

260

261   **NECAP clamps AP2 in a closed, inactive conformation**

262   Our structural, genetic, and biochemical data suggest a mechanism whereby NECAP

263   clamps AP2 in a closed, inactive conformation via simultaneous engagement of the mu and beta

264   subunits. We tested this hypothesis using our *in vitro* protease sensitivity assay. We incubated

265   open phosphoAP2 with NECAP and found that including NECAP decreases the protease

266   sensitivity of AP2, consistent with the closed conformation observed in our structure (Figure 7A,

267   top). Additionally, by comparing various truncations of NECAP we found that both $NECAP_{PHear}$

268   and $NECAP_{Ex}$ were required for this activity (Figure 7A). When we measured the protease

269   sensitivity of endogenous AP2 in *C. elegans* expressing NECAP truncations, we saw a similar

270   dependence on $NECAP_{PHearEx}$ for full function (Figure 7A, bottom). Additionally, we observed

271   that $NECAP_{PHearEx}$ was sufficient to rescue a NECAP deletion in worms using our whole animal

272   fitness assay (Figure 7B). Taken together, these data show that $NECAP_{PHearEx}$ locks AP2 into an

273   inactivated conformation.

274

275   **Discussion**

276   Our combination of genetic, biochemical, and structural data supports a mechanism by

277   which NECAP inactivates AP2 by initially recognizing open, unphosphorylated complexes and

278   promoting the closed, inactive conformation after phosphorylation (Figure 7C). Previous work in

279   vertebrate tissue culture suggests that NECAP$_{Tail}$ mediates binding of AP2 through the alpha

280   appendage (Ritter et al., 2003). However, NECAP$_{Tail}$ is poorly conserved in *C. elegans* (Figure

281   1B) and is dispensable for activity in our assays (Figure 7A, B) (Beacham et al., 2018). This

282   suggests that we have found an additional and perhaps more ancient activity of NECAP, by

283   which the conserved NECAP$_{PHear}$ and NECAP$_{Ex}$ domains cooperate to stabilize the closed

284   conformation of AP2 in a three-step cycle (Figure 7C). First, AP2 complexes are recruited to the

285   plasma membrane where PIP$_2$ and other activators induce the opening and stabilization of the

286   complex (Höning et al., 2005). Next, NECAP$_{Ex}$ recognizes open AP2 complexes and binds to the

287   beta subunit, placing NECAP$_{PHear}$ close to AP2 at a high local concentration. Finally, after AP2

288   phosphorylation, NECAP$_{PHear}$ engages the mu subunit of AP2 to clamp the complex in a state

289   resistant to activation (Figure 7). Our data confirm this complex is closed despite the otherwise

290   activating signal of membrane mimetics (Figure 5B) and is resistant to proteolysis (Figure 7A).

291   Importantly, this inactivation cycle has a strong dependence on phosphorylation of AP2 (Figure

292   3), suggesting that inactivation of AP2 is a tightly regulated mechanism.

293   While we have uncovered new molecular details of how an endocytic regulator can

294   inactivate the AP2 complex, how this process is controlled both spatially and temporally remains

295   an open question. One possibility is that NECAP action is dictated by the timing of AP2 kinase

296   recruitment or activation (Conner et al., 2003; Jackson et al., 2003) and that AP2 complexes

297   become inactivated by NECAP immediately upon phosphorylation. Another possibility is that

298   NECAP cannot inactivate stabilized AP2 complexes, but only complexes that are not yet fully

299   initiated, thereby serving as a quality control mechanism (Aguet et al., 2013; Cocucci et al.,

300   2012; Ehrlich et al., 2004; Puthenveedu and von Zastrow, 2006). However, NECAP is reported

301   at endocytic structures (Sochacki et al., 2017) coincident with the arrival of clathrin (Taylor et

302 al., 2011), suggesting that NECAP may act later in the endocytic cycle, after AP2 activation.

303 More speculatively, it is possible that clathrin adaptor inactivation may be involved in vesicle

304 uncoating, as closed AP2 complexes cannot interact with cargo (Collins et al., 2002; Jackson et

305 al., 2010; Kelly et al., 2008) and a clathrin-binding motif on the beta hinge is occluded in this

306 conformation (Kelly et al., 2014). It is also not clear whether NECAP has functions apart from

307 regulation of AP2. For example, the phosphorylated threonine of the AP2 mu subunit is

308 conserved on the mu subunit of AP1 (Ghosh and Kornfeld, 2003; Heldwein et al., 2004; Ren et

309 al., 2013) and NECAP has been proposed to both interact with and control AP1 (Chamberland et

310 al., 2016; Ritter et al., 2004). This suggests a broader role for NECAP and regulated adaptor

311 inactivation at other membrane compartments.

325 **Declaration of interests:** The authors declare no competing interests.

326 **Figure titles and legends**

327 **Figure 1. NECAP PHear domain binds phosphorylated AP2 core.**

328 (A) AP2 comprises four subunits: alpha (α), beta (β), mu (μ), and sigma (σ). The complex also

329 comprises a structured 'core' (dashed box) connected by flexible linkers to appendages on the

330 alpha and beta subunits. Binding sites for AP2 substrates are indicated. PIP_2,

331 PhosphatidylInositol-4,5-bisPhosphate. (B) (Top) NECAP domain organization (numbers are for

332 human NECAP2). (Center) Conservation scores of NECAP residues calculated using the

333 ConSurf server (Ashkenazy et al., 2010; Celniker et al., 2013). (Bottom) Truncation constructs

334 used in this work. (C) Binding analysis of NECAP truncations compared to HaloTag control (-).

335 HT, HaloTag; phosphoAP2, phosphorylated AP2 core. Representative image of three technical

336 replicates. (D) Cryo-EM map of the phosphoAP2-NECAP complex (PDB 6OWO). Red:

337 NECAP; Blue: AP2 mu; Grey: AP2 alpha, beta, sigma. See also Figure 1—figure supplement 1

338 and Figure 1—figure supplement 2.

339

340 **Figure 2. Genetic screen for NECAP-AP2 interface mutations.**

341 (A) Schematic of genetic screen to identify residues important for AP2-NECAP binding. FCHo

342 mutants (*fcho-1*) exhibit growth defect and 'jowls' phenotype due to inactive AP2 (cartoon is

343 anterior of worm). Fluorescent tag on NECAP (RFP:NECAP) enables visual categorization of

344 suppressor mutations that restore AP2 activity. (B) Mutations identified in (A) mapped as red

345 spheres onto the subunits of the closed AP2 crystal structure (2VGL) and our NECAP$_{PHear}$ cryo-

346 EM structure (PDB 6OWO). (C) Table of *C. elegans* mutations and their vertebrate equivalents

347 referenced in this manuscript.

348

349

Figure 3. Coordination of phosphorylated AP2 by NECAP is required for inactivation.

(A) Cryo-EM of phosphoAP2-NECAP complex, boxed region shown in (B). (B) phosphoAP2-

NECAP interface as a ribbon diagram inside a transparent rendering of the cryo-EM map with

ball-and-stick representation of relevant NECAP side chains and mu pT156. Red: NECAP; Blue:

AP2-mu. See also Figure 3—figure supplement 1. (C) Binding analysis of interface mutants

compared to HaloTag control (–). HT, HaloTag. Representative image of two technical

replicates. (D) In the absence of NECAP (–), *fcho-1* mutants take about 4 days to proliferate and

consume a bacterial food source (fitness defect = 0). Expression of NECAP (+) increases the

number of days to about 8 (fitness defect = 1). Data for interface mutants were normalized to this

fitness defect; n = 10 biological replicates. (E) (Left) In *fcho-1; apm-2 (E306K)* mutant worms,

NECAP is recruited to the nerve ring. Interface mutants disrupt nerve ring recruitment, as

quantified by *in vivo* confocal microscopy. (Right) Normalized RFP intensities plotted above

representative confocal nerve ring images of ten biological replicates. (D-E) Error bars indicate

mean ± SEM. Significance compared to NECAP (+); Student's t-test performed on raw data (D)

or normalized data (E). *P < 0.05, **P < 0.01, ***P < 0.001, ****P < 0.0001. (F) *In vivo*

protease sensitivity assay to probe AP2 conformation in genetic backgrounds indicated. In the

absence of NECAP (–), AP2 is protease sensitive (open). Expression of wild type NECAP (+)

results in protease resistant AP2 (closed). All strains lack *fcho-1*.

368   **Figure 4. Membrane mimetics stimulate opening of AP2.**

369   (A) Schematic of protease sensitivity assay. Open AP2 exposes thrombin site on mu. K, mu

370   E302K mutation. (B) Protease sensitivity of AP2 (mu E302K) in the presence of anionic

371   polymers. Oligo, 60 nucleotide single-stranded DNA; plasmid, double-stranded DNA; RNA,

372   total yeast RNA; IP6: inositol hexakisphosphate. (C) AP2 crystal structures (left, PDB 2VGL;

373   right, PDB 2XA7) (D) (Top) Representative AP2 cryo-EM 2D class averages in the absence

374   (left) or presence of oligo (47 nucleotide single-stranded DNA, right). (Bottom) Images from

375   above overlaid with closed (left) or open (right) AP2 crystal structures. Blue: AP2 mu. The C-

376   terminal domain of mu was omitted from the open crystal structure, as it is disordered in our

377   cryo-EM class averages. (E) Proportion of AP2 particles assigned to either closed (grey) or open

378   (blue) class averages. Data represents ten technical replicates (see definition of technical

379   replicates for this assay in methods). See also Figure 4—figure supplement 1. (F) Binding

380   analysis of NECAP to AP2 (mu E302K) in the presence or absence of heparin. HT, HaloTag; K,

381   mu E302K mutation. HaloTag control (-). Representative image of three technical replicates.

382

383   **Figure 5. NECAP$_{Ex}$ recognizes membrane-activated AP2.**

384   (A) Binding analysis of NECAP truncations to AP2 (mu E302K) in the presence of heparin.

385   HaloTag control (-). Representative image of two technical replicates. (B) Cryo-EM density of

386   the phosphorylated AP2 (mu E302K)-NECAP complex in the presence of oligo (PDB 6OXL, 47

387   nucleotide single-stranded DNA, 5 molar excess). See also Figure 5—figure supplement 1,

388   Figure 5—figure supplement 2.

389

390

391 **Figure 6. The AP2-NECAP$_{Ex}$ interface is required for inactivation.**

392 (A) Residues identified in our genetic screen (see Figure 2) shown as colored spheres on a ribbon

393 diagram of AP2 with outline of NECAP$_{Ex}$ density (red, low isosurface threshold, see Figure 6—

394 figure supplement 1). (B) Binding curves generated from pulldown depletion assays. Error bars

395 represent mean ± SEM from three technical replicates. Inset: Calculated K$_d$ values, variance is

396 SEM. *P < 0.05, **P < 0.01, relative to control. (C) In the absence of NECAP (–), *fcho-1*

397 mutants take about 4 days to proliferate and consume a bacterial food source (fitness defect = 0).

398 Expression of NECAP (+) increases the number of days to about 8 (fitness defect = 1). Data for

399 interface mutants were normalized to this fitness defect; n = 10 biological replicates. (D) In *fcho-*

400 *1; apm-2 (E306K)* mutant worms, NECAP is recruited to the nerve ring. Interface mutants

401 disrupt nerve ring recruitment. Normalized RFP intensities plotted above representative confocal

402 nerve ring images of ten biological replicates. (C-D) Error bars indicate mean ± SEM.

403 Significance compared to NECAP (+); Student's t-test performed on raw data (C) or normalized

404 data (D). *P < 0.05, **P < 0.01, ***P < 0.001, ****P < 0.0001. (E) *In vivo* protease sensitivity

405 assay to probe AP2 conformation in genetic backgrounds indicated. In the absence of NECAP

406 (–), AP2 is protease sensitive (open). Expression of wild type NECAP (+) results in protease

407 resistant AP2 (closed). All strains lack *fcho-1*. See also Figure 6—figure supplement 1.

408

409 **Figure 7. NECAP clamps AP2 in a closed, inactive conformation.**

410 (A) Analysis of NECAP activity on AP2 protease sensitivity. (Left) Schematic of components.

411 Oligo, 60 nucleotide single-stranded DNA. (Center) Samples analyzed by western blot to

412 quantify cleavage of mu subunit. (Right) Western blots cropped to show uncut mu subunit after

413 either addition of protease (*in vitro*, top) or protease expression via heat shock promoter (*in vivo*,

414   bottom). Numbers represent normalized intensity of the uncut mu band, relative to the sample

415   with full length NECAP. (B) In the absence of NECAP (–), *fcho-1* mutants take about 4 days to

416   proliferate and consume a bacterial food source (fitness defect = 0). Expression of NECAP (Full

417   length) increases the number of days to about 8 (fitness defect = 1). Data for the truncations were

418   normalized to this fitness defect; n = 10 biological replicates. ***P < 0.001; ns, not significant;

419   relative to NECAP knockout (-). N=10 biological replicates. (C) Model of AP2 inactivation by

420   NECAP.

421

422   **Supplemental figure titles and legends**

423   **Figure 1—figure supplement 1. Classification, signal subtraction, and refinement of**

424   **phosphoAP2 bound to NECAP**

425   (A) Representative 2D class averages demonstrating different particle orientation preferences

426   under different grid preparation conditions. (B) Processing workflow for 3D classification and

427   refinement of phosphoAP2-NECAP using the Relion 3 software suite. (C) Cryo-EM map colored

428   by local resolution (Relion 3). (D) Fourier Shell Correlation (FSC) plot. (E) 3D FSC plot. An

429   overall sphericity of 0.95 shows that resolution is nearly uniform in three dimensions. (F)

430   Histogram plot of Cα RMSD of top ten molecular models from Rosetta refinement. Inset shows

431   molecular model colored and scaled by RMSD.

432

433   **Figure 1—figure supplement 2. Comparison of NECAP solution structure and**

434   **phosphoAP2-NECAP cryo-EM structure**

435   (A) Cryo-EM map of phosphoAP2-NECAP is shown with a solid surface (left) and with a

436   transparent surface with the closed AP2 crystal structure docked (middle). Masking the region

437   corresponding to AP2 and subtracting this density from the full map gives a psuedo difference

438   density map (right). (B) Solution structure of NECAP$_{PHear}$ (PDB 1TQZ) docked into the

439   difference density from (A). NECAP$_{PHear}$ comprises a single alpha helix and beta sheet, which

440   can be clearly seen in the cryo-EM density. However, the solution structure has some

441   conformational differences compared to the AP2-bound cryo-EM structure. (C) The molecular

442   model for NECAP$_{PHear}$ and AP2 mu (AA 154-158) are shown in the cryo-EM density. PDB

443   1TQZ was used as a starting model to manually rebuild in Coot and refine using Rosetta.

444

445   **Figure 3—figure supplement 1. Comparison of NECAP binding site in open and closed**

446   **AP2 conformations.**

447   (A) phosphoAP2-NECAP structure. The mu subunit is colored blue, with residues 154-170

448   colored cyan, and pT156 colored magenta. NECAP$_{PHear}$ is colored red. (B) Model of open AP2

449   bound to NECAP$_{PHear}$ colored as in (A). NECAP$_{PHear}$ was docked onto the open AP2

450   conformation (PDB 2XA7) by aligning the mu homology domain (AA 160-435) of the two

451   models. The NECAP$_{PHear}$ binding site on the mu subunit is solvent exposed in both structures,

452   except the mu linker packs against beta in the open conformation, including T156. (C) Model of

453   open AP2 bound to NECAP as shown boxed in (B). The location of muT156 is highlighted for

454   the phosphoAP2-NECAP structure and the open AP2 structure. While there are no steric clashes

455   preventing NECAP binding to open AP2, access to and phosphorylation of muT156 is a key

456   determinant of NECAP binding.

457

458   **Figure 4—figure supplement 1. Cryo-EM analysis of AP2 in the presence of an anionic**

459   **polymer (DNA).**

460   (A) 2D class averages for WT AP2 + DNA are shown. Averages corresponding to the closed

461   conformation (red inset) and open conformation (blue inset) are shown next to their respective

462   molecular models (PDB 2VGL; PDB 2XA7). (B) 3D classification shows that the dataset

463   contains a mixture of open and closed conformations. Classification was performed in Relion 3.

464   Resolution is limited for all open structures because of an extreme preferred orientation in the

465   cryo-EM grids. (C). Representative 2D class averages from AP2 samples. Mutations and the

466   presence of DNA are labeled. DNA is in a 5-fold molar excess. Closed 2D classes are boxed in

467   red, open 2D classes are boxed in blue. (D) Binding curve of phosphoAP2 (mu E302K)-NECAP

468   and a 47 bp ssDNA oligo. 20 nM DNA was incubated with increasing amounts of phosphoAP2-

469   NECAP. A native gel shift assay was used to measure binding. Data was plotted and analyzed

470   using the Prism software package.

471

472   **Figure 5—figure supplement 1. Cryo-EM data collection, processing, and model building**

473   **for phosphoAP2-NECAP-DNA 'clamped' structure.**

474   (A) Representative motion-corrected, dose-weighted cryo-EM micrographs of phosphoAP2-

475   NECAP-DNA complex. (B) Classification and refinement pipeline used for structure

476   determination. Particles were extracted and 2D classified in Relion3. 'Clean' particles were re-

477   extracted and used for ab initio model generation and refinement in cryoSPARC v2. 2D and 3D

478   FSC plots are shown for the final model. (C) Final cryo-EM structure colored by local resolution.

479   (D) Histogram plot of Cα RMSD of top ten molecular models from Rosetta refinement. Inset

480   shows molecular model colored and scaled by RMSD.

481

482   **Figure 6—figure supplement 1. The NECAP$_{Ex}$ domain binds along the surface of the beta**

483   **subunit.**

484   (A) The unfiltered, refined cryo-EM map of 'clamped' phosphoAP2-NECAP is shown at

485   different isosurface threshold levels (top). A psuedo difference density map was made in

486   Chimera by masking the region corresponding to AP2 and subtracting this map from the full map

487   (bottom). The remaining density is shown colored salmon. The same threshold levels are shown

488   top and bottom. (B) The psuedo difference density from (A) is shown at a low threshold level

489   and with a Gaussian filter applied. Regions of the map corresponding to obvious AP2 features,

490   such as loops omitted from our molecular model, were manually removed in Chimera. We

491   hypothesize that a region of NECAP$_{Ex}$ cryo-EM density (boxed in red) corresponds to a

492   conserved region of the sequence called the KEG motif (AA 153-154) . This is consistent with

493   structural restraints based on the distance of this motif (16 residues) from the C-terminus of

494   NECAP$_{PHear}$ in our molecular model (AA 8-137).

495

496   **Figure 5—figure supplement 2. Structural comparison of 'unclamped' and 'clamped'**

497   **phosphoAP2-NECAP structures.**

498   (A) Cartoon diagram of phosphoAP2-NECAP 'unclamped' structure. NECAP is not shown.

499   Top: AP2 subunits are colored as labeled. Bottom: AP2 is colored by per-residue RMSD. Values

500   were calculated in PyMol using whole-molecule alignment of 'unclamped' vs 'clamped'

501   phosphoAP2-NECAP. (B) Cryo-EM maps of 'unclamped' (top) and 'clamped' (bottom)

502   phosphoAP2-NECAP structures. Maps were locally filtered by local resolution to standardize

503   comparison between maps. Cryo-EM density corresponding to beta AA 404-474 is shown

504   (right). Both maps are colored by local resolution using the same color gradient (color key in

505   (C)). (C) The NECAP$_{Ex}$ binding site (beta AA 404-474) is shown for the 'unclamped'

506   phosphoAP2-NECAP (top) and 'clamped' phosphoAP2-NECAP (bottom) structures. A small

507   region of beta partially melts when the Ex domain is bound.

508 **MODEL SYSTEM**

509 *C. elegans* **Strains**

510 A complete strain list used in this study is provided in the Key Resources Table.

511 An annotated strains list is included in supplemental file 1.

512 *C. elegans* **maintenance**

513 *C. elegans* were maintained at room temperature (22-25°C) using standard procedures (Brenner,

514 1974) on nematode growth medium (NGM) plates seeded with *E. coli* strain OP50. All animals

515 used in this study were larval stage 4 (L4) or young adult (3-4 days old) hermaphrodites.

516

517 **METHOD DETAILS**

518 **Fitness assay**

519 Fitness (starvation) assays were performed as previously described (Hollopeter et al., 2014).

520 Briefly, three young adult *C. elegans* hermaphrodites were placed on NGM plates with bacterial

521 food source. The number of days for the population of worms to expand and consume the food

522 was recorded.

523 **Transgenic strains**

524 Generation of transgenic strains by CRISPR was performed as previously described (Beacham et

525 al., 2018) using ribonucleoprotein complexes (Paix et al., 2015). Injection mixes contained 19

526 μM recombinant Cas9 nuclease (purified in-house), 30 μM crispr RNA (crRNA) for desired edit

527   (IDT), 35 µM trans-activating crRNA (trRNA, IDT), 6 µM crRNA targeting the *dpy-10* locus

528   (IDT), and 2.5 µM *dpy-10 (rol)* single stranded oligo repair template (IDT). For small missense

529   mutations, 10 µM single-stranded oligonucleotide (oligo) DNA repair template (IDT) was

530   included. For large insertions, such as fluorophores, repair templates (PCR products with 35 base

531   pair homology arms flanking the Cas9 cleavage site) were included at a final concentration of 1

532   µM. Gonad arms of young adult hermaphrodite *C. elegans* were injected and *rol* F1 offspring of

533   the injected worms were transferred to a fresh plate, allowed to lay eggs, and genotyped for the

534   desired edit. Non-*rol* F2 offspring were similarly screened to isolate worms with homozygous

535   edits. GUN89 was generated using mos1-mediated single copy insertion as previously described

536   (Beacham et al., 2018; Frøkjær-Jensen et al., 2012) by injecting targeting vector pEP57 into *C.*

537   *elegans* strain EG6703.

Mutagenesis screen

539   *C. elegans* strains GUN61 or GUN88 (*fcho-1* mutants expressing *RFP:NECAP*) were

540   mutagenized in 0.5 mM N-nitroso-N-ethylurea (ENU, Sigma Aldrich N3385) for 4 hr at 22 °C.

541   After washing with M9 buffer, animals were distributed onto growth plates (10 cm NGM plates

542   seeded with concentrated bacterial OP50 culture). Once the worm population had expanded and

543   consumed the food source, ~2 × 2 cm pieces of each plate were transferred to a fresh growth

544   plate. This process was repeated 4-6 times to select for genotypes with greater fitness, which

545   were then visually screened to eliminate NECAP knockouts (RFP negative) and open AP2

546   mutations (nerve-ring-enriched RFP). Genomic regions corresponding to AP2 subunits and

547   NECAP were amplified by PCR and sequenced in candidate interface mutants. To confirm that

548   the mutations we identified were responsible for the observed phenotypes, we generated them *de*

549   *novo* using CRISPR.

550 **Recombinant protein purification**

551 *AP2 complex purification*

552 AP2 cores were purified as described previously (Hollopeter et al., 2014) with some

553 modifications. Plasmids encoding wild type or mutant AP2 cores were expressed in *E. coli*

554 (BL21 DE3, NEB). To generate phosphorylated AP2 cores, a plasmid encoding the kinase

555 domain of AAK1 was included. *E. coli* cultures (500-6000 mL) expressing the AP2 cores were

556 lysed by sonication in 50 mM Tris pH 8.0, 1000 mM NaCl, 10% glycerol, 10 mM $MgCl_2$, 1 mM

557 $CaCl_2$, 150 ng/μL lysozyme (Sigma), 24 ng/μL DNAse (grade II from bovine pancreas, Roche),

558 1mM Phenylmethylsulfonyl fluoride (PMSF), and one cOmplete EDTA-free Protease Inhibitor

559 Cocktail tablet (Roche). Clarified lysate was passed over a column packed with GST resin to

560 bind AP2. Column was washed with 50 mM Tris pH 8.0, 1000 mM NaCl, 10% glycerol, and 1

561 mM DTT until optical density at 280 nm (OD280) of the flow-through was below 0.05 arbitrary

562 units (AU). Column was then washed in TBS-DTT (20 mM Tris pH 7.6, 150 mM sodium

563 chloride, and 1 mM DTT) prior to elution. Complexes were eluted using glutathione elution

564 buffer (50 mM Tris, 150 mM sodium chloride, 10mM reduced glutathione, 1 mM DTT, final pH

565 9.0) or treated with GST-HRV protease (purified in-house) to release AP2 from the GST affinity

566 tag. Eluted complexes were buffer-exchanged with TBS-DTT and concentrated by centrifugal

567 filtration to 1-5 μM before snap-freezing in liquid nitrogen for long-term storage.

568 *Hexahistidine-tagged (6xHis) protein Purification*

569 Hexahistidine-tagged proteins were purified as described previously (Beacham et al., 2018;

570 Hollopeter et al., 2014) with some modifications. *E. coli (*BL21 DE3, NEB; 500 mL culture)

571 expressing hexahistidine-tagged proteins were lysed by sonication in 50 mM Tris pH 8.0, 500

572   mM NaCl, 10% glycerol, 10 mM MgCl$_2$, 1 mM CaCl$_2$, 150 ng/µL lysozyme (Sigma), 24 ng/µL

573   DNAse (grade II from bovine pancreas, Roche), 1 mM PMSF, and one cOmplete EDTA-free

574   Protease Inhibitor Cocktail tablet (Roche). Clarified lysate was passed over a column packed

575   with TALON resin (Clontech) to bind the hexahistidine-tagged protein. The column was first

576   washed with 50 mM Tris pH 8.0, 500 mM NaCl, 10% glycerol, and 5 mM BME until the OD280

577   of the flow-through was below 0.05 AU. Column was then washed with TBS-BME (20 mM Tris

578   pH 7.6, 150 mM sodium chloride, and 5 mM BME), and the bound protein was eluted using

579   TBS-BME supplemented with 150mM imidazole. Proteins were buffer exchanged with TBS-

580   DTT and concentrated to 100 µM by centrifugal filtration before snap-freezing in liquid nitrogen

581   for long-term storage.

582   *phosphoAP2-NECAP purification*

583   *E. coli* (BL21 DE3, NEB; 500 - 6000 mL culture) expressing phosphoAP2 core

584   (pGH504/pGH419/pEP82) or phosphoAP2 (mu E302K) core (pGH504/pGB106/pEP82) were

585   prepared as in *AP2 complex purification* above, until after the wash steps. Before elution, 10 mg

586   purified mouse NECAP2:6xHis (pGH503) was flowed over the resin in a total volume of 25 mL

587   TBS-DTT. Column was washed in 50 mM Tris pH 8.0, 500 mM NaCl, 10% glycerol, 5 mM

588   BME. The complex was released from the GST affinity tag by incubation with GST-HRV

589   protease (purified in-house). The phosphoAP2-NECAP complex was further purified using a

590   column packed with TALON resin to remove AP2 that was not bound to 6xHis-tagged NECAP.

591   Column was washed with 50 mM Tris pH 8.0, 500 mM NaCl, 10% glycerol, 5 mM BME. The

592   complex was eluted using 50 mM Tris pH 8.0, 500 mM NaCl, 10% glycerol, and 5 mM BME

593   supplemented with 150 mM imidazole. The sample was concentrated to OD280 of ~4 AU and

594   further purified using gel filtration (Superdex 200 Increase 10/300 GL column, General Electric).

595   The sample was buffer exchanged with 20 mM HEPES pH 8.0, 150 mM KCl, 1 mM DTT during

596   gel filtration. The final complex was concentrated to >10 μM before snap-freezing in liquid

597   nitrogen for long-term storage.

598   ***In vitro* pulldowns**

599   Pulldown assays were performed essentially as described (Hollopeter et al., 2014) except the

600   protease cleavage step was 3-6 hr. For the pulldown assay, 80 pmol of purified HaloTag:NECAP

601   bait or HaloTag control, 40 pmol of recombinant AP2 prey, and 10 μL of Magne HaloTag Bead

602   slurry (20%, Promega) were mixed in TBS-DTT (1 mL total volume for each pulldown) and

603   nutated overnight at 4°C. For pulldowns with 'open AP2', 100 μg heparin was also included.

604   After incubation, the beads were washed with TBS-DTT and bound proteins were cleaved from

605   the HaloTag by incubation with TEV protease (purified in-house, 3-6 hr at 22°C). Eluted

606   proteins were visualized by coomassie-stained sodium dodecyl sulfate polyacrylamide gel

607   electrophoresis (SDS-PAGE). Images in manuscript are cropped to show the largest AP2 band

608   for each prey (alpha:GST, or alpha and beta).

609   **Pulldown depletion assay**

610   To determine the K_d of NECAP for open AP2, we measured how much AP2 was precipitated by

611   various concentrations of immobilized NECAP. Open AP2 (50 nM AP2 mu E302K with 10

612   ng/μL heparin) was incubated with HaloTag:NECAP2:6xHis (30-3000 nM) and TALON

613   hexahistidine affinity resin (20 μL) in TBS-T (20 mM Tris pH 7.6, 150 mM NaCl with 0.1%

614   Tween-20, final reaction volume 100 μL). Samples were agitated at 1500 rpm for one hour at 22

615   °C. The resin was allowed to settle and 45 μL of the supernatant was analyzed by coomassie-

616   stained SDS-PAGE.

617 **_In vitro_ protease assay**

618 This assay was used to measure the conformation of AP2 complexes _in vitro_. A thrombin

619 protease site (DNA sequence 5'-ctggtgccgcgcggcagc-3') was inserted into the mu subunit after

620 residue S236. This protease site becomes exposed when AP2 adopts the open conformation. To

621 perform the assay, 20 pmol of purified AP2, 3.3μg of activators (oligo DNA, plasmid DNA,

622 RNA, or heparin), and 50 pmol of HaloTag:NECAP or 50 pmol of HaloTag control were mixed

623 in 30 μL TBS-DTT. Thrombin protease (Sigma T7009, 3 μL) was then added (see amounts and

624 timings below). Reactions were incubated at 22° C for 10 minutes (0.25 U thrombin, Figure 4B)

625 or 30 minutes (0.5 U thrombin, all others) and terminated by addition of 11μL 4X Bolt LDS

626 Sample Buffer (ThermoFisher) and incubation at 95° C for 5 minutes. Cleavage of the mu

627 subunit was analyzed by coomassie-stained SDS-PAGE (Figure 4B) or by western blot for the

628 phosphorylated mu subunit (Figure 7A, top). The primary antibody was rabbit anti-AP2M1

629 phospho T156 (1:1000, Abcam 109397), and the secondary antibody was goat anti-rabbit Alexa

630 Fluor 647 (1:2000, Life Technologies, A21244).

631 **_In vivo_ protease assay**

632 _In vivo_ TEV assays were performed as previously described (Beacham et al., 2018). _C. elegans_

633 strains used in this assay express heat-shock inducible TEV protease and an AP2 mu transgene

634 containing a TEV protease site that is exposed specifically when AP2 is in an open

635 conformation. The strains also express an RFP:NECAP transgene or RFP alone. 100 L4 stage _C._

636 _elegans_ hermaphrodites were picked from a growth plate either before or 6 hr after a 1 hr heat

637 shock (34° C). Worms were placed in 1 mL of 20 mM Tris pH 7.6, 150 mM NaCl (TBS) with

638 0.001% Triton X-100. Animals were pelleted at 1000 g and washed once with TBS containing

639   0.001% Triton X-100. Samples were pelleted again and the supernatant removed, leaving behind

640   45 μL total volume. 15 μL 4x Bolt LDS Sample Buffer supplemented with fresh dithiothreitol

641   (DTT) was added, and sample was snap frozen in liquid nitrogen. Samples were then lysed in a

642   cup horn sonicator (Branson Ultrasonics Corporation, Danbury, CT; 1 s pulses at 90–95%

643   amplitude for 2–3 min) followed by heating to 70 °C for 10 minutes. Samples were re-sonicated

644   following the 70˚C denaturation step if any exhibited excessive viscosity. The entire sample was

645   separated by SDS-PAGE and western blot analysis was performed to detect the 3xFLAG-tagged

646   mu subunit. The primary antibody was mouse anti-flag (1:1000, Sigma-Aldrich F3165), and the

647   secondary antibody was goat anti-mouse IRDye 800CW (1:20000, LI-COR, 925-32210).

648   *In vivo* **imaging assay**

649   Nerve ring imaging was performed as previously described (Beacham et al., 2018) with

650   modifications to data quantification. Live worms were immobilized on slides and imaged on a

651   Zeiss LSM 880 confocal microscope with a 40x water immersion objective. Fluorophores were

652   excited with 488 nm (GFP) and 561 nm (RFP) lasers. Strains for each experiment were imaged

653   in one session with the same laser settings. For each worm, a single confocal slice through the

654   approximate sagittal section of the nerve ring was analyzed in Fiji. The GFP-AP2 signal

655   corresponding to the nerve ring was used to define a region of interest (ROI) for quantification of

656   'nerve ring RFP'. A second ROI in the anterior of the worm that was outside the nerve ring and

657   pharynx was used for normalization.

658   **Cryo-EM structure determination**

659   The following conditions were used for all cryo-EM samples. Grids were prepared by glow

660   discharging UltraAuFoil R 1.2/1.3 300 mesh gold grids (Quantifoil GmbH) for 30 seconds at 20

661   mAmp. Grids were used within 10 minutes of charging. 4 μL of sample was applied to grids and

662   plunge frozen in liquid ethane using a Vitrobot Mark IV robot (Thermo Fisher) set to 100%

663   humidity, 4°C, blot force 20, and blot time 4 s. Samples were imaged using a Talos Arctica TEM

664   (Thermo Fisher) operating at 200 keV in nano probe mode and equipped with a K2 Summit

665   Direct Electron Detector (Thermo Fisher). Parallel illumination of the microscope was performed

666   according to (Herzik et al., 2017). Images were collected at 36,000x, yielding a final pixel size of

667   1.16 Å for counting mode and 0.58 Å for super resolution mode. Dose fractionated movies were

668   collected at a defocus range of -0.6 μm and -2.5 μm and an exposure rate of ~6 e-/pixel/s with

669   200 ms frames and a total exposure of ~50 e-/Å^2. New camera gain references were collected

670   before each dataset and the hardware dark reference was updated daily. The microscope was

671   operated using the Leginon software suite (Suloway et al., 2005) and data were processed on the

672   fly using the Appion software suite (Lander et al., 2009), including motion correction and gain

673   correction using MotionCor2 (Zheng et al., 2017), CTF estimation using CTFFIND4 (Rohou and

674   Grigorieff, 2015), and particle picking using DogPicker.py (Voss et al., 2009). Particles were

675   extracted from dose-weighted, aligned micrographs and analyzed using cryoSPARC (Punjani et

676   al., 2017) and Relion-3 (Nakane et al., 2018). Unless otherwise noted, resolution values are

677   according to the 0.143 gold standard Fourier shell correlation (GSFSC) method (Scheres, 2012).

678   *phosphoAP2-NECAP cryo-EM structure determination*

679   The phosphorylated AP2 core was purified in complex with full-length mouse NECAP2 using

680   recombinant expression in *E. coli* and used to make cryo-EM grids (see *phosphoAP2-NECAP*

681   *purification*, above). The final protein buffer was 20 mM HEPES-KCl, pH 8.0, 150 mM KCl, 1

682   mM DTT. We noticed that particles had a different orientation in the ice based on protein

683   concentration and/or the presence of a detergent, n-Octyl-β-D-Glucopyranoside (β-OG) (Figure

684   1—figure supplement 1A). To increase the angular distribution of the particles in the final

685   dataset, three datasets (5 µM protein, 1 µM protein, and 5 µM protein + 0.05% w/v β-OG) were

686   collected using the same exposure rate, total exposure, frame rate, and magnification, then

687   merged and processed as a single dataset. A total of 1092 movies were collected and 944

688   remained after removing micrographs with crystalline ice or CTF fits worse than 3.5 Å as judged

689   by the 0.5 criterion in Appion. 890,658 particles were extracted, subjected to multiple rounds of

690   2D classification and re-extraction in Relion-3, yielding a dataset of 490,560 'clean' particles.

691   These particles were used to generate an *ab initio* 3D model in cryoSPARC, which was used as a

692   search model for 3D classification and 3D auto-refinement in Relion-3. After masking and

693   postprocessing, this yielded a 3.7 Å resolution map. After local CTF refinement and beam-tilt

694   estimation in Relion-3, the resolution improved to 2.9 Å resolution. While the AP2 core was well

695   resolved, the density for NECAP was lower resolution (~4.5 Å local resolution), preventing us

696   from building an accurate model. Signal subtraction (Bai et al., 2015) and 3D classification

697   without alignment were used to find a sub-population that refined to 3.2 Å resolution, but with

698   significantly improved density for NECAP. Local resolution estimation was performed using

699   Relion-3, showing a range from 3.1 to 4.2 Å resolution, with the bulk of the model below 3.5 Å.

700   This final map was used for model building, see *Model building and validation*, below.

701   *phosphoAP2-NECAP (mu E302K) + DNA cryo-EM structure determination*

702   The phosphorylated AP2 core containing a hyper-active mu E302K mutation was purified in

703   complex with full-length mouse NECAP2 using recombinant expression in *E. coli* (see

704   *phosphoAP2-NECAP purification* above). The final protein buffer was 20 mM HEPES-KCl, pH

705   8.0, 150 mM KCl, 1 mM DTT, 0.05% w/v β-OG. phosphoAP2-NECAP (mu E302K) at 3 µM

706   concentration was mixed with 15 μM of a 60 bp single-stranded DNA oligo (oEP971) and used

707   to make cryo-EM grids. A total of 1497 movies were collected and 1126 remained after

708   removing micrographs with crystalline ice or CTF fits worse than 3.5 Å. 717,231 particles were

709   extracted, subjected to multiple rounds of 2D classification and re-extraction in Relion-3,

710   yielding a dataset of 388,962 'clean' particles. These particles were used to generate an *ab initio*

711   3D model in cryoSPARC. 324,922 particles were found to go into high-resolution classes using

712   heterogeneous refinement, and a final refinement was performed using the non-uniform

713   refinement protocol in cryoSPARC v2, yielding a final resolution of 3.5 Å. Map sharpening and

714   local resolution estimation was performed using cryoSPARC v2.

715   *Model building and validation*

716   For each AP2-NECAP complex, the same general process was followed. The crystal structure of

717   the AP2 complex in the closed conformation (PDB 2VGL) (Collins et al., 2002) and the solution

718   structure of mouse NECAP1 (PDB 1TQZ) (Ritter et al., 2007) were docked into the cryo-EM

719   map using Chimera (Pettersen et al., 2004). First, NECAP was manually rebuilt in Coot to match

720   the cryo-EM density. A round of real space refinement was performed in Phenix using

721   phenix.real_space_refine (Afonine et al., 2018). Regions of AP2 absent from the PDB 2VGL

722   model were manually built in Coot (Emsley and Cowtan, 2004), including a region of the mu

723   subunit containing phosphorylated T156. The NECAP model was then improved using

724   RosettaCM and Rosetta *FastRelax* integrated into a cloud-based cryo-EM pipeline (Cianfrocco et

725   al., 2018; Wang et al., 2015, 2016). At this point, a full phosphoAP2-NECAP model was

726   generated and used as a starting model to generate ~1000 models using RosettaCM. The model

727   with the lowest energy score was then used to generate 100 models in Rosetta *FastRelax*. The

728   lowest energy model from this analysis was further refined using phenix.real_space_refine. For

729   the 'unclamped' phosphoAP2-NECAP model, the following side chains were truncated to the Cβ

730   atom (alpha residue 11; beta residue 5; mu residue 253, 261, 379, 380; NECAP residues 62,

731   102). For the 'clamped' phosphoAP2-NECAP model, the following side chains were truncated to

732   the Cβ atom (alpha residue 11, 123, 217, 341, 381; beta residue 5, 26, 27, 232; mu residue 21,

733   26, 261, 281, 379, 380; NECAP residues 94, 101, 102, 137). Additionally, a short poly-alanine

734   peptide was modeled into the NECAP$_{Ex}$ density and included during model refinement for the

735   'clamped' structure.

736   *2D classification of 'open' vs 'closed' AP2 complexes*

737   AP2 and AP2 (mu E302K) were purified using recombinant expression in *E. coli* (see *AP2*

738   *complex purification* above). Cryo-EM grids were prepared with 3 μM protein with or without a

739   5x molar excess of a 60 bp single-stranded DNA oligo (oEP971, same as that used in protease

740   assay). Gel shift assays showed that phosphoAP2 (mu E302K)-NECAP has a Kd of ~60 nM for

741   the DNA oligo used for cryo-EM (Figure S4D). Assuming a single binding site, AP2 is expected

742   to be >98% bound at the concentrations used for our cryo-EM analysis. Four datasets in total

743   were collected: AP2, AP2 + DNA, AP2 (mu E302K), AP2 (mu E302K) + DNA. Particles were

744   extracted and analyzed in Relion-3. For each sample, we first performed several rounds of 2D

745   classification, yielding about ~50% of particles that entered classes with well-resolved secondary

746   structure.

747

748

749

750   **QUANTIFICATION AND STATISTICAL ANALYSIS**

751   **Fitness Assays**

752   Measurements of number of days to starve were taken from 10 biological replicates for each

753   strain. Significance was calculated using an unpaired, two tailed T-test with Prism GraphPad

754   software. Data was normalized relative to NECAP (-) and NECAP (+) strains for visualization

755   only.

756   **Pulldown Depletion Assays**

757   Three technical replicates were performed for each sample. Alpha:GST band intensity was

758   quantified ($AP2^{MEASURED}$) and these values were plotted against NECAP concentrations on a

759   logarithmic scale. A sigmoidal (4PL) fit was applied to the data using GraphPad Prism 7.04. The

760   asymptote representing the maximum AP2 that would remain in solution at zero NECAP

761   concentration was calculated ($AP2^{MAX}$). The 'fraction AP2 bound' in each sample was then

762   calculated using the formula ($1 - [AP2^{MEASURED}/AP2^{MAX}]$). These normalized values were then

763   plotted against NECAP concentrations on a logarithmic scale and an EC50 (K_d) was calculated

764   from a sigmoidal (4PL) fit of the data using GraphPad Prism 7.04. Note that for Figure 6B,

765   'fraction AP2 bound' was plotted against the concentration of NECAP on a linear scale.

766   ***In vivo* Imaging Assays**

767   Strains for each experiment were imaged in one session with the same laser settings. For each

768   worm, a single confocal slice through the approximate sagittal section of the nerve ring was

769   analyzed in Fiji. The GFP-AP2 signal corresponding to the nerve ring was used to define a

770   region of interest (ROI) for quantification of 'nerve ring RFP'. A second ROI in the anterior of

771   the worm that was outside the nerve ring and pharynx was used for normalization. 'Nerve ring

772   RFP' was quantified as the average fluorescent intensity in the nerve ring ROI divided by the

773   average fluorescent intensity in the ROI for normalization. Images were analyzed for ten

774   biological replicates, and significance was calculated using an unpaired, two tailed T-test with

775   Prism GraphPad software.

776   **2D classification of 'open' versus 'closed' AP2 complexes**

777   After identifying particles that fit into well-defined 2D classes, each particle set was randomly

778   split into 10 subsets (technical replicates) and 2D classified in Relion-3. For each random subset,

779   classes were divided into 'open' or 'closed' conformations based on projection matching with

780   the 'open' (PDB 2XA7) (Jackson et al., 2010) and 'closed' (PDB 2VGL) (Collins et al., 2002)

781   crystal structures. Projection matching was performed in SPIDER (Frank et al., 1996) with in-

782   house scripts. The ten measurements of 'open' vs. 'closed' were used to calculate a standard

783   error of the mean (SEM).

784

785   **DATA AND CODE AVAILABILITY**

786   The density maps generated during this study are available at the Electron Microscopy Data

787   Bank (EMD-20215, unclamped and EMD-20220, clamped); the atomic structures generated

788   during this study are available at the Protein Data Bank (PDB 6OWO, unclamped and 6OXL,

789   clamped).

790

References

Afonine, P.V., Poon, B.K., Read, R.J., Sobolev, O.V., Terwilliger, T.C., Urzhumtsev, A., and Adams, P.D. (2018). Real-space refinement in PHENIX for cryo-EM and crystallography. Acta Crystallogr D Struct Biol *74*, 531–544.

Aguet, F., Antonescu, C.N., Mettlen, M., Schmid, S.L., and Danuser, G. (2013). Advances in analysis of low signal-to-noise images link dynamin and AP2 to the functions of an endocytic checkpoint. Dev. Cell *26*, 279–291.

Aguilar, R.C., Ohno, H., Roche, K.W., and Bonifacino, J.S. (1997). Functional Domain Mapping of the Clathrin-associated Adaptor Medium Chains µ1 and µ2. J. Biol. Chem. *272*, 27160–27166.

Ashkenazy, H., Erez, E., Martz, E., Pupko, T., and Ben-Tal, N. (2010). ConSurf 2010: calculating evolutionary conservation in sequence and structure of proteins and nucleic acids. Nucleic Acids Res. *38*, W529–W533.

Bai, X.-C., Rajendra, E., Yang, G., Shi, Y., and Scheres, S.H.W. (2015). Sampling the conformational space of the catalytic subunit of human γ-secretase. Elife *4*.

Beacham, G.M., Partlow, E.A., Lange, J.J., and Hollopeter, G. (2018). NECAPs are negative regulators of the AP2 clathrin adaptor complex. Elife *7*.

Brenner, S. (1974). The genetics of Caenorhabditis elegans. Genetics *77*, 71–94.

Celniker, G., Nimrod, G., Ashkenazy, H., Glaser, F., Martz, E., Mayrose, I., Pupko, T., and Ben-Tal, N. (2013). ConSurf: Using Evolutionary Data to Raise Testable Hypotheses about Protein Function. Isr. J. Chem. *53*, 199–206.

811   Chamberland, J.P., Antonow, L.T., Dias Santos, M., and Ritter, B. (2016). NECAP2 controls

812   clathrin coat recruitment to early endosomes for fast endocytic recycling. J. Cell Sci. *129*, 2625–

813   2637.

814   Cianfrocco, M.A., Lahiri, I., DiMaio, F., and Leschziner, A.E. (2018). cryoem-cloud-tools: A

815   software platform to deploy and manage cryo-EM jobs in the cloud. J. Struct. Biol. *203*, 230–

816   235.

817   Cocucci, E., Aguet, F., Boulant, S., and Kirchhausen, T. (2012). The first five seconds in the life

818   of a clathrin-coated pit. Cell *150*, 495–507.

819   Collins, B.M., McCoy, A.J., Kent, H.M., Evans, P.R., and Owen, D.J. (2002). Molecular

820   architecture and functional model of the endocytic AP2 complex. Cell *109*, 523–535.

821   Conner, S.D., and Schmid, S.L. (2002). Identification of an adaptor-associated kinase, AAK1, as

822   a regulator of clathrin-mediated endocytosis. J. Cell Biol. *156*, 921–929.

823   Conner, S.D., Schröter, T., and Schmid, S.L. (2003). AAK1-Mediated μ2 Phosphorylation is

824   Stimulated by Assembled Clathrin. Traffic *4*, 885–890.

825   Cremona, O., Di Paolo, G., Wenk, M.R., Lüthi, A., Kim, W.T., Takei, K., Daniell, L., Nemoto,

826   Y., Shears, S.B., Flavell, R.A., et al. (1999). Essential role of phosphoinositide metabolism in

827   synaptic vesicle recycling. Cell *99*, 179–188.

828   Ehrlich, M., Boll, W., Van Oijen, A., Hariharan, R., Chandran, K., Nibert, M.L., and

829   Kirchhausen, T. (2004). Endocytosis by random initiation and stabilization of clathrin-coated

830   pits. Cell *118*, 591–605.

831   Emsley, P., and Cowtan, K. (2004). Coot: model-building tools for molecular graphics. Acta

832   Crystallogr. D Biol. Crystallogr. *60*, 2126–2132.

833   Fingerhut, A., von Figura, K., and Honing, S. (2001). Binding of AP2 to sorting signals is

834   modulated by AP2 phosphorylation. J. Biol. Chem. *276*, 5476–5482.

835   Frank, J., Radermacher, M., Penczek, P., Zhu, J., Li, Y., Ladjadj, M., and Leith, A. (1996).

836   SPIDER and WEB: processing and visualization of images in 3D electron microscopy and

837   related fields. J. Struct. Biol. *116*, 190–199.

838   Frøkjær-Jensen, C., Davis, M.W., Ailion, M., and Jorgensen, E.M. (2012). Improved Mos1-

839   mediated transgenesis in C. elegans. Nat. Methods *9*, 117–118.

840   Ghosh, P., and Kornfeld, S. (2003). AP-1 binding to sorting signals and release from clathrin-

841   coated vesicles is regulated by phosphorylation. J. Cell Biol. *160*, 699–708.

842   Hannan, L.A., Newmyer, S.L., and Schmid, S.L. (1998). ATP- and cytosol-dependent release of

843   adaptor proteins from clathrin-coated vesicles: A dual role for Hsc70. Mol. Biol. Cell *9*, 2217–

844   2229.

845   He, K., Marsland, R., III, Upadhyayula, S., Song, E., Dang, S., Capraro, B.R., Wang, W.,

846   Skillern, W., Gaudin, R., Ma, M., et al. (2017). Dynamics of phosphoinositide conversion in

847   clathrin-mediated endocytic traffic. Nature *552*, 410–414.

848   Heldwein, E.E., Macia, E., Wang, J., Yin, H.L., Kirchhausen, T., and Harrison, S.C. (2004).

849   Crystal structure of the clathrin adaptor protein 1 core. Proc. Natl. Acad. Sci. U. S. A. *101*,

850   14108–14113.

851 Henne, W.M., Boucrot, E., Meinecke, M., Evergren, E., Vallis, Y., Mittal, R., and McMahon,

852 H.T. (2010). FCHo proteins are nucleators of clathrin-mediated endocytosis. Science *328*, 1281–

853 1284.

854 Herzik, M.A., Jr, Wu, M., and Lander, G.C. (2017). Achieving better-than-3-Å resolution by

855 single-particle cryo-EM at 200 keV. Nat. Methods *14*, 1075–1078.

856 Hollopeter, G., Lange, J.J., Zhang, Y., Vu, T.N., Gu, M., Ailion, M., Lambie, E.J., Slaughter,

857 B.D., Unruh, J.R., Florens, L., et al. (2014). The membrane-associated proteins FCHo and SGIP

858 are allosteric activators of the AP2 clathrin adaptor complex. Elife *3*.

859 Höning, S., Ricotta, D., Krauss, M., Späte, K., Spolaore, B., Motley, A., Robinson, M.,

860 Robinson, C., Haucke, V., and Owen, D.J. (2005). Phosphatidylinositol- (4,5)-bisphosphate

861 regulates sorting signal recognition by the clathrin-associated adaptor complex AP2. Mol. Cell

862 *18*, 519–531.

863 Jackson, A.P., Flett, A., Smythe, C., Hufton, L., Wettey, F.R., and Smythe, E. (2003). Clathrin

864 promotes incorporation of cargo into coated pits by activation of the AP2 adaptor micro2 kinase.

865 J. Cell Biol. *163*, 231–236.

866 Jackson, L.P., Kelly, B.T., McCoy, A.J., Gaffry, T., James, L.C., Collins, B.M., Höning, S.,

867 Evans, P.R., and Owen, D.J. (2010). A large-scale conformational change couples membrane

868 recruitment to cargo binding in the AP2 clathrin adaptor complex. Cell *141*, 1220–1229.

869 Jia, X., Weber, E., Tokarev, A., Lewinski, M., Rizk, M., Suarez, M., Guatelli, J., and Xiong, Y.

870 (2014). Structural basis of HIV-1 Vpu-mediated BST2 antagonism via hijacking of the clathrin

871 adaptor protein complex 1. Elife *3*, e02362.

872   Kadlecova, Z., Spielman, S.J., Loerke, D., Mohanakrishnan, A., Reed, D.K., and Schmid, S.L.

873   (2017). Regulation of clathrin-mediated endocytosis by hierarchical allosteric activation of AP2.

874   J. Cell Biol. *216*, 167–179.

875   Kelly, B.T., McCoy, A.J., Späte, K., Miller, S.E., Evans, P.R., Höning, S., and Owen, D.J.

876   (2008). A structural explanation for the binding of endocytic dileucine motifs by the AP2

877   complex. Nature *456*, 976–979.

878   Kelly, B.T., Graham, S.C., Liska, N., Dannhauser, P.N., Höning, S., Ungewickell, E.J., and

879   Owen, D.J. (2014). Clathrin adaptors. AP2 controls clathrin polymerization with a membrane-

880   activated switch. Science *345*, 459–463.

881   Kirchhausen, T., Owen, D., and Harrison, S.C. (2014). Molecular structure, function, and

882   dynamics of clathrin-mediated membrane traffic. Cold Spring Harb. Perspect. Biol. *6*, a016725.

883   Lander, G.C., Stagg, S.M., Voss, N.R., Cheng, A., Fellmann, D., Pulokas, J., Yoshioka, C.,

884   Irving, C., Mulder, A., Lau, P.-W., et al. (2009). Appion: an integrated, database-driven pipeline

885   to facilitate EM image processing. J. Struct. Biol. *166*, 95–102.

886   Loerke, D., Mettlen, M., Yarar, D., Jaqaman, K., Jaqaman, H., Danuser, G., and Schmid, S.L.

887   (2009). Cargo and dynamin regulate clathrin-coated pit maturation. PLoS Biol. *7*, e57.

888   Matsui, W., and Kirchhausen, T. (1990). Stabilization of clathrin coats by the core of the

889   clathrin-associated protein complex AP-2. Biochemistry *29*, 10791–10798.

890   Mettlen, M., Chen, P.-H., Srinivasan, S., Danuser, G., and Schmid, S.L. (2018). Regulation of

891   Clathrin-Mediated Endocytosis. Annu. Rev. Biochem. *87*, 871–896.

892   Nakane, T., Kimanius, D., Lindahl, E., and Scheres, S.H. (2018). Characterisation of molecular

893   motions in cryo-EM single-particle data by multi-body refinement in RELION. Elife *7*.

894   Olusanya, O., Andrews, P.D., Swedlow, J.R., and Smythe, E. (2001). Phosphorylation of

895   threonine 156 of the μ2 subunit of the AP2 complex is essential for endocytosis in vitro and in

896   vivo. Curr. Biol. *11*, 896–900.

897   Owen, D.J., Collins, B.M., and Evans, P.R. (2004). Adaptors for clathrin coats: structure and

898   function. Annu. Rev. Cell Dev. Biol. *20*, 153–191.

899   Paix, A., Folkmann, A., Rasoloson, D., and Seydoux, G. (2015). High Efficiency, Homology-

900   Directed Genome Editing in Caenorhabditis elegans Using CRISPR-Cas9 Ribonucleoprotein

901   Complexes. Genetics *201*, 47–54.

902   Pauloin, A., Bernier, I., and Jollès, P. (1982). Presence of cyclic micleotide–Ca2+ independent

903   protein kinase in bovine brain coated vesicles. Nature *298*, 574–576.

904   Pettersen, E.F., Goddard, T.D., Huang, C.C., Couch, G.S., Greenblatt, D.M., Meng, E.C., and

905   Ferrin, T.E. (2004). UCSF Chimera—a visualization system for exploratory research and

906   analysis. J. Comput. Chem. *25*, 1605–1612.

907   Punjani, A., Rubinstein, J.L., Fleet, D.J., and Brubaker, M.A. (2017). cryoSPARC: algorithms

908   for rapid unsupervised cryo-EM structure determination. Nat. Methods *14*, 290–296.

909   Puthenveedu, M.A., and von Zastrow, M. (2006). Cargo regulates clathrin-coated pit dynamics.

910   Cell *127*, 113–124.

911   Ren, X., Farías, G.G., Canagarajah, B.J., Bonifacino, J.S., and Hurley, J.H. (2013). Structural

912   basis for recruitment and activation of the AP-1 clathrin adaptor complex by Arf1. Cell *152*,

913   755–767.

914   Ricotta, D., Conner, S.D., Schmid, S.L., von Figura, K., and Höning, S. (2002). Phosphorylation

915   of the AP2 μ subunit by AAK1 mediates high affinity binding to membrane protein sorting

916   signals. J. Cell Biol. *156*, 791–795.

917   Ritter, B., Philie, J., Girard, M., Tung, E.C., Blondeau, F., and McPherson, P.S. (2003).

918   Identification of a family of endocytic proteins that define a new α-adaptin ear-binding motif.

919   EMBO Rep. *4*, 1089–1093.

920   Ritter, B., Denisov, A.Y., Philie, J., Deprez, C., Tung, E.C., Gehring, K., and McPherson, P.S.

921   (2004). Two WXXF-based motifs in NECAPs define the specificity of accessory protein binding

922   to AP-1 and AP-2. EMBO J. *23*, 3701–3710.

923   Ritter, B., Denisov, A.Y., Philie, J., Allaire, P.D., Legendre-Guillemin, V., Zylbergold, P.,

924   Gehring, K., and McPherson, P.S. (2007). The NECAP PHear domain increases clathrin

925   accessory protein binding potential. EMBO J. *26*, 4066–4077.

926   Ritter, B., Murphy, S., Dokainish, H., Girard, M., Gudheti, M.V., Kozlov, G., Halin, M., Philie,

927   J., Jorgensen, E.M., Gehring, K., et al. (2013). NECAP 1 regulates AP-2 interactions to control

928   vesicle size, number, and cargo during clathrin-mediated endocytosis. PLoS Biol. *11*, e1001670.

929   Rohou, A., and Grigorieff, N. (2015). CTFFIND4: Fast and accurate defocus estimation from

930   electron micrographs. J. Struct. Biol. *192*, 216–221.

931   Scheres, S.H.W. (2012). RELION: implementation of a Bayesian approach to cryo-EM structure

932   determination. J. Struct. Biol. *180*, 519–530.

933   Sochacki, K.A., Dickey, A.M., Strub, M.-P., and Taraska, J.W. (2017). Endocytic proteins are

934   partitioned at the edge of the clathrin lattice in mammalian cells. Nat. Cell Biol. *19*, 352–361.

935   Suloway, C., Pulokas, J., Fellmann, D., Cheng, A., Guerra, F., Quispe, J., Stagg, S., Potter, C.S.,

936   and Carragher, B. (2005). Automated molecular microscopy: the new Leginon system. J. Struct.

937   Biol. *151*, 41–60.

938   Taylor, M.J., Perrais, D., and Merrifield, C.J. (2011). A high precision survey of the molecular

939   dynamics of mammalian clathrin-mediated endocytosis. PLoS Biol. *9*, e1000604.

940   Umasankar, P.K., Ma, L., Thieman, J.R., Jha, A., Doray, B., Watkins, S.C., and Traub, L.M.

941   (2014). A clathrin coat assembly role for the muniscin protein central linker revealed by

942   TALEN-mediated gene editing. Elife *3*.

943   Umeda, A., Meyerholz, A., and Ungewickell, E. (2000). Identification of the universal cofactor

944   (auxilin 2) in clathrin coat dissociation. Eur. J. Cell Biol. *79*, 336–342.

945   Voss, N.R., Yoshioka, C.K., Radermacher, M., Potter, C.S., and Carragher, B. (2009). DoG

946   Picker and TiltPicker: software tools to facilitate particle selection in single particle electron

947   microscopy. J. Struct. Biol. *166*, 205–213.

948   Wang, R.Y.-R., Kudryashev, M., Li, X., Egelman, E.H., Basler, M., Cheng, Y., Baker, D., and

949   DiMaio, F. (2015). De novo protein structure determination from near-atomic-resolution cryo-

950   EM maps. Nat. Methods *12*, 335–338.

951   Wang, R.Y.-R., Song, Y., Barad, B.A., Cheng, Y., Fraser, J.S., and DiMaio, F. (2016).

952   Automated structure refinement of macromolecular assemblies from cryo-EM maps using

953   Rosetta. Elife *5*.

954   Zheng, S.Q., Palovcak, E., Armache, J.-P., Verba, K.A., Cheng, Y., and Agard, D.A. (2017).

955   MotionCor2: anisotropic correction of beam-induced motion for improved cryo-electron

956   microscopy. Nat. Methods *14*, 331–332.

957

Table 1. Cryo-EM data collection, refinement, and validation statistics

	pAP2-NECAP "unclamped"		pAP2-NECAP "clamped"	
	PDB ID:	6OWO	PDB ID:	6OXL
	EMDB ID:	EMD-20215	EMDB ID:	EMD-20220
Data Collection				
Microscope	Talos Arctica		Talos Arctica	
Camera	K2 summit		K2 summit	
Camera Mode	Super-Resolution		Counting	
Magnification	36,000		36,000	
Voltage (kV)	200		200	
Total electron exposure (e-/Å2)	60		50	
Exposure rate (e-/pixel/sec)	6.67		6.43	
Defocus Range (um)	0.6-2.5		0.6-2.5	
Pixel Size (Å/pixel)	0.58		1.16	
Micrographs collected (no.)	1092		1497	
Micrographs used (no.)	944		1126	
Reconstruction				
3D Processing Package	Relion 3		cryoSPARC v2	
Total Extracted picks (no.)	890,658		717,231	
Refined particles (no.)	490,560		388,962	
Final Particles (no.)	71,571		324,922	
Symmetry	C1		C1	
Resolution (global) (Å)	3.2		3.5	
FSC 0.143 (unmasked/masked)	4.1/3.2		(4.2/3.5)	
Local resolution range (Å)	3.1-4.2		3.2-6.1	
Map sharpening B-factor	-29		-160	
Refinement				
Model refinement package	Rosetta, phenix.real_space_refine		Rosetta, phenix.real_space_refine	
Model composition				
Nonhydrogen atoms	14,280		14,418	
Protein residues	1,785		1,814	
B factors (Å2)				
Protein residues	62.53		62.72	
R.m.s. deviations				
Bond Lengths (Å)	0.009		0.01	
Bond angles (°)	1.182		1.253	
Validation				
MolProbity score	1.4		1.75	
Clashscore	3.92		6.62	
Poor rotamers (%)	0.25		0.06	
CaBLAM outliers (%)	1.34		1.38	
Ramachandran plot				
Favored (%)	96.57		94.36	
Allowed (%)	3.32		5.64	
Disallowed (%)	0.11		0	
EMRinger score	3.33		3.047	
Map CC ($CCmask$)	0.857		0.815	

Figure 1. NECAP PHear domain binds phosphorylated AP2 core.

A closed (inactive) open (active)

core

appendages

M membrane (PIP$_2$) binding ■ clathrin binding
C cargo binding P phosphorylation site

B

NECAP — PHear | Ex | Tail (1, 132, 170, 263)

Conservation

Full Length
Conserved
PHearEx
PHear
ExTail

C *In vitro* pulldowns

HaloTag:NECAP truncation

HaloTag: NECAP (bait) + Phospho-AP2 (prey)

–, Full Length, Conserved, PHearEx, PHear, ExTail

D

AP2
NECAP$_{PHear}$
AP2 (mu)
90°

Figure 2. Genetic screen for NECAP-AP2 interface mutations.

A Mutagenize worms — Passage worms many generations — Classify *fcho-1* suppressors (active AP2)

'jowls' (inactive AP2)

fcho-1 RFP:NECAP

Mutations that suppress *fcho-1* confer fitness advantage.

I. RFP recruited to nerve ring → Open AP2 mutant ✗

II. RFP negative → NECAP knockout ✗

III. RFP diffuse → Candidate interface mutant ✓

B NECAP_PHear — NECAP S87N — AP2 (core) +NECAP — AP2 (mu)

AP2 (sigma)

Linker — mu T156A (x6) — mu T156I (x2) — Mu domain

AP2 (core)

AP2 (alpha) — AP2 (beta)

alpha I470D — beta A447P (x3)

C

Gene	Amino acid change	Mouse equivalent	Isolation method		
			This screen	Previously	Other
mu (*apm-2*)	T160A	T156A Ⓟ	6x	once	–
mu (*apm-2*)	T160I	T156I Ⓟ	twice	once	–
NECAP (*ncap-1*)	S84N	S87N	once	once	–
NECAP (ncap-1)	R109E	R112E	–	–	predicted
NECAP (*ncap-1*)	A29D	A32D	–	once	–
alpha (*apa-2*)	V469D	I470D	once	–	–
beta (*apb-1*)	S444P	S447P	thrice	–	–
NECAP (ncap-1)	KEG148-150AAA	KDG153-155AAA	–	–	predicted
mu (*apm-2*)	E306K	E302K	–	–	open AP2

Figure 3. Coordination of phosphorylated AP2 by NECAP is required for inactivation.

A

B

NECAP$_{PHear}$ A32   S87   R112   mu $\textcircled{P}$ T156

C *In vitro* pulldowns

HaloTag: NECAP (bait) + Phospho-AP2 (prey)

NECAP:	-	+	+	S87N	R112E
AP2:	+	+	mu T156A	+	+
AP2 (prey):					

D *In vivo* fitness assay

Place 3 animals on growth plate

NECAP activity = reduced fitness
fcho-1

Quantify # of days for food to be depleted

Loss of NECAP = increased fitness
fcho-1 ncap-1

Population expands and consumes food

Fitness Defect

**** **** **** ****

-	+	mu T160A	NECAP S84N	NECAP R109E
NECAP				

fcho-1 ncap-1

E *In vivo* imaging assay

AP2 (mu E306K) recruits NECAP to the nerve ring in *C. elegans*

fcho-1 ncap-1; apm-2(E306K) + NCAP-1:RFP

90°   90°

Confocal slice

Nerve ring RFP (AU)

* ** **

-	+	mu T160A	NECAP S84N	NECAP R109E
NECAP				

fcho-1 ncap-1; apm-2(muE306K)

F *In vivo* protease sensitivity

open AP2

AP2 (mu) western

open   closed

Uncut

Cut

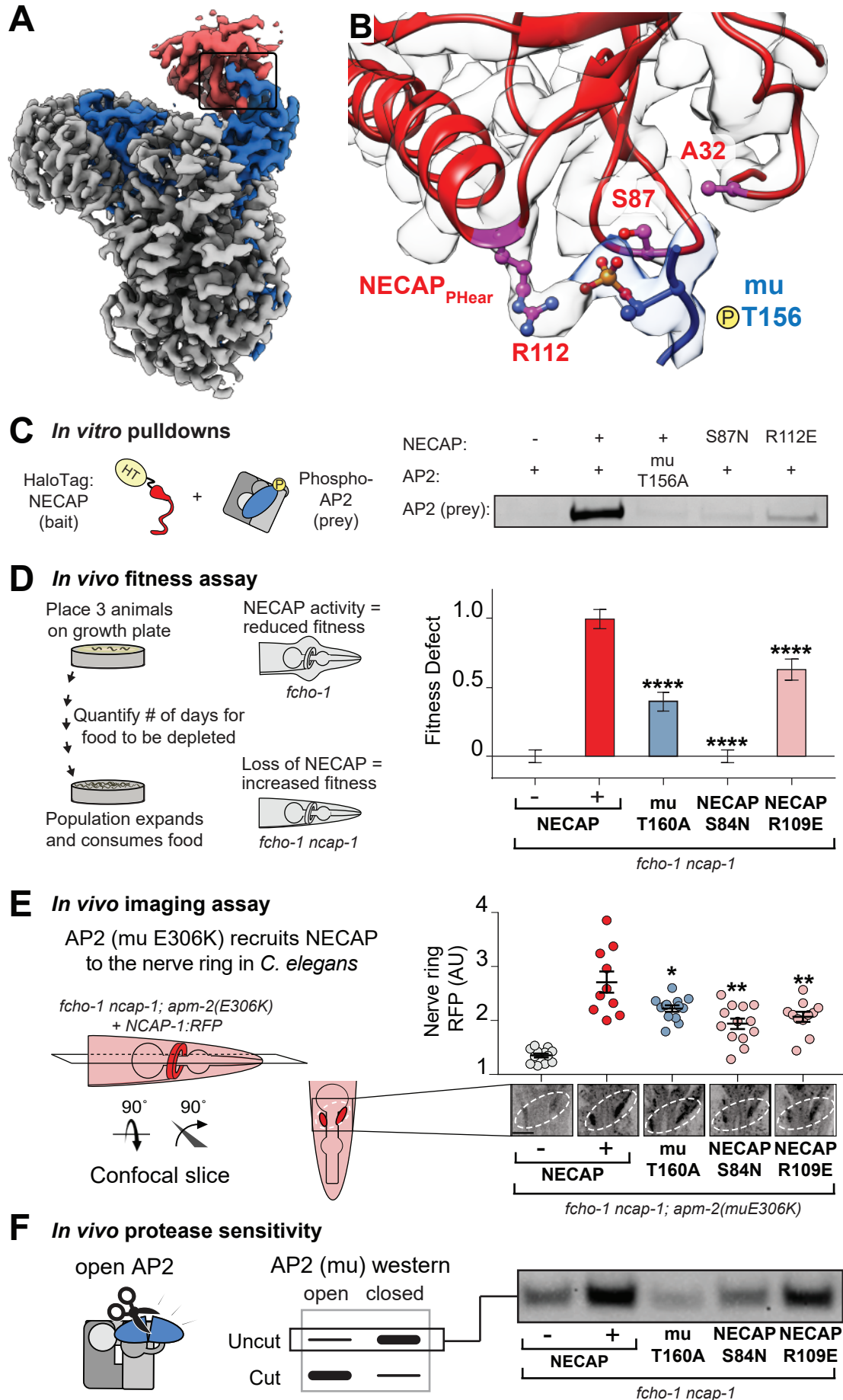| -	+	mu T160A	NECAP S84N	NECAP R109E
NECAP				

fcho-1 ncap-1

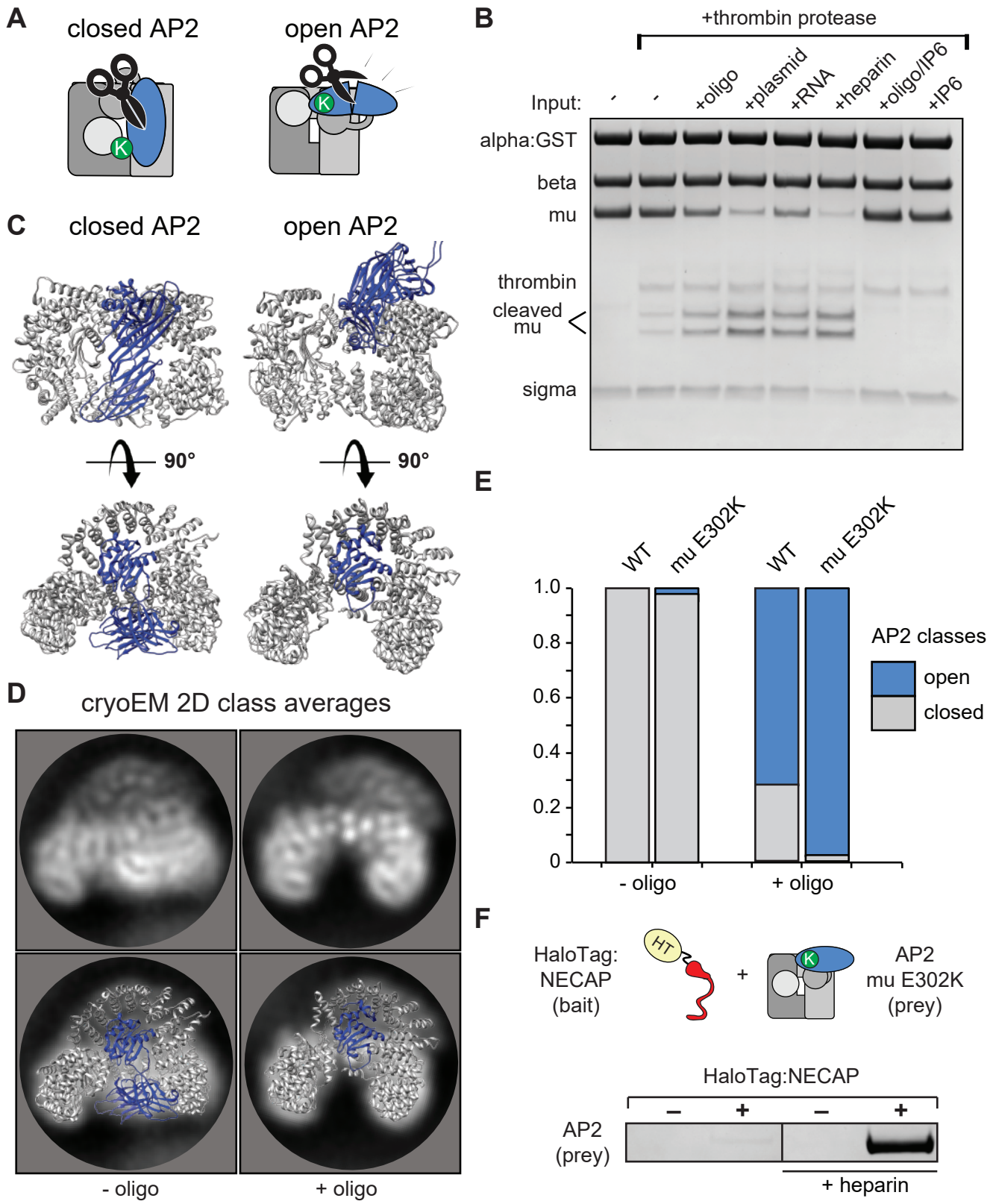# Figure 4. Membrane-mimetics stimulate opening of AP2.

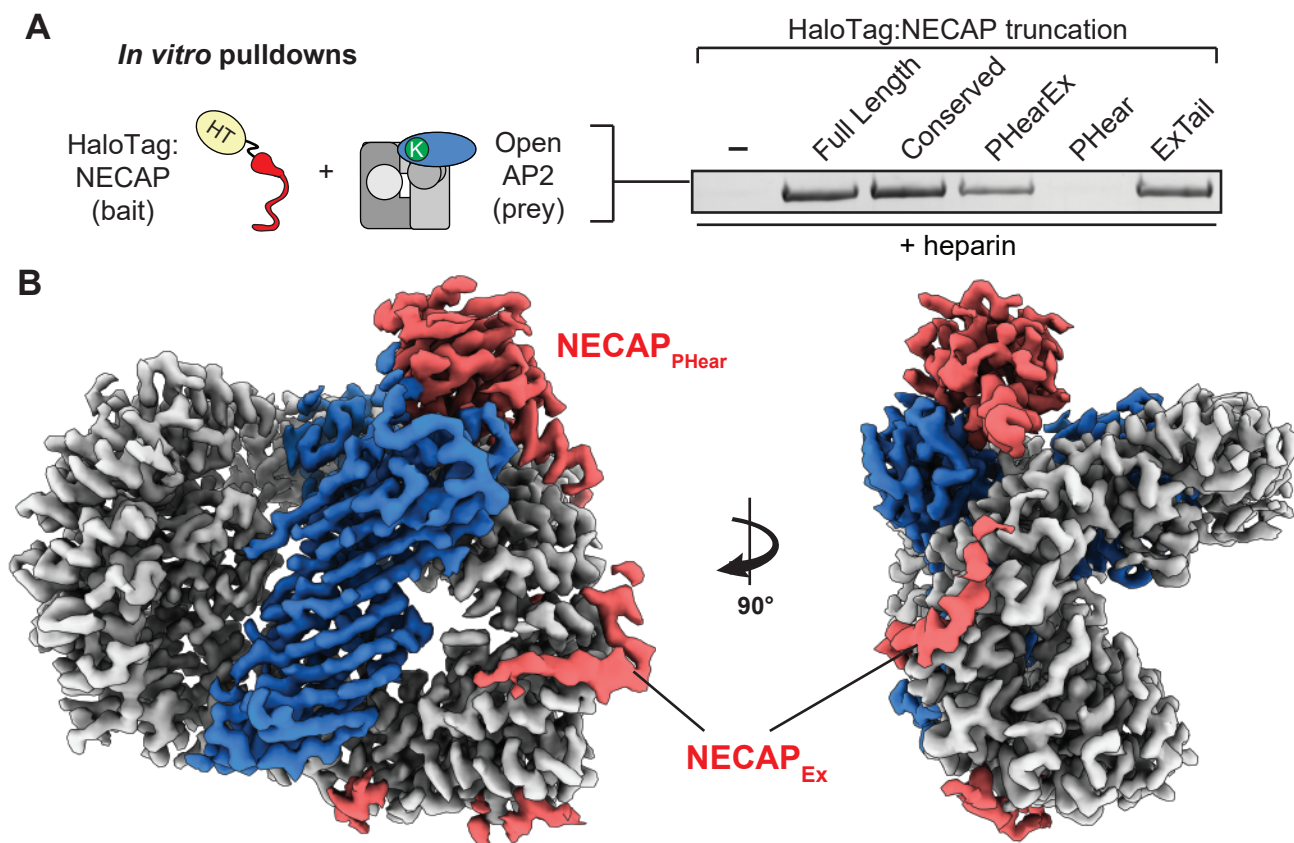# Figure 5. NECAP$_{Ex}$ recognizes membrane-activated AP2.

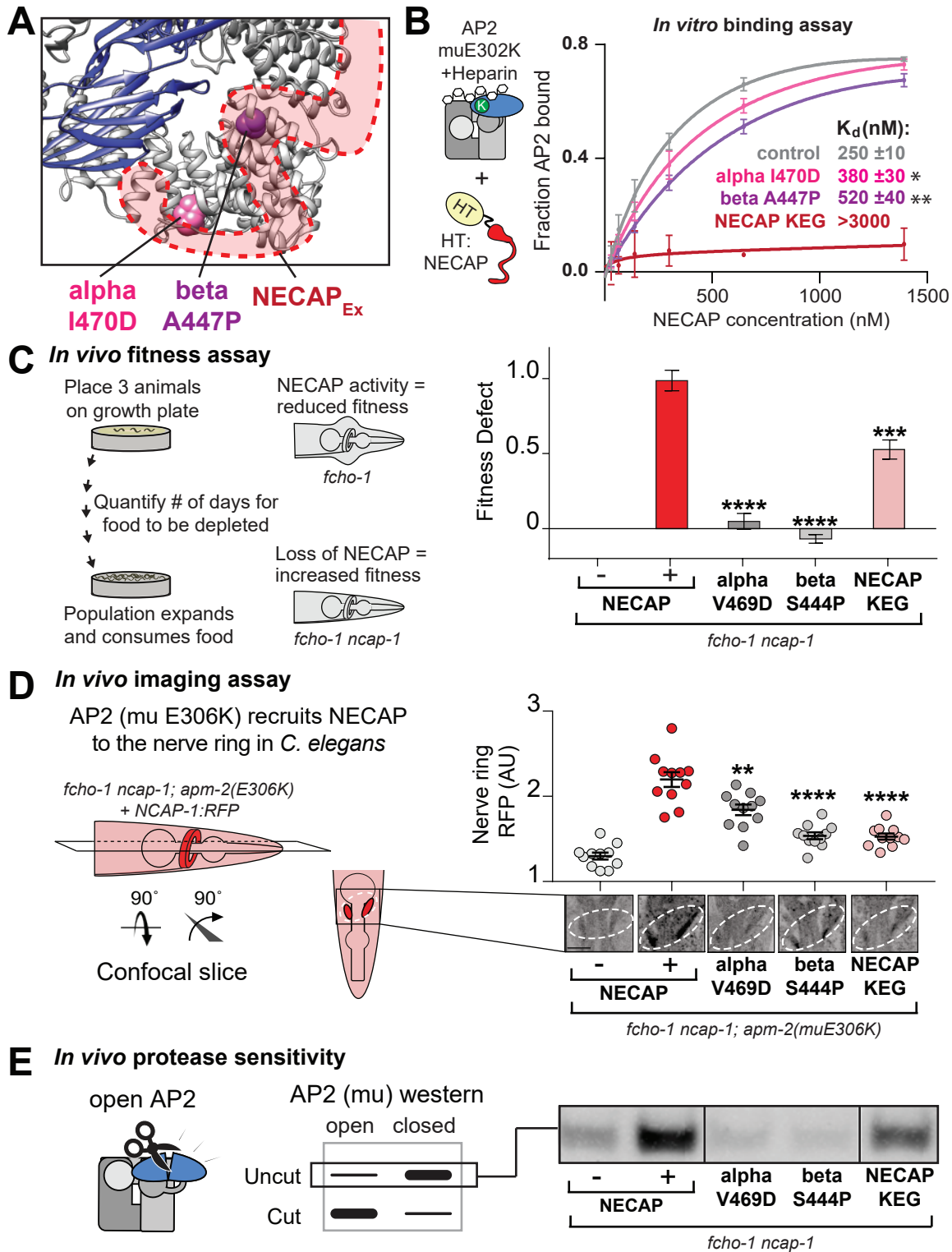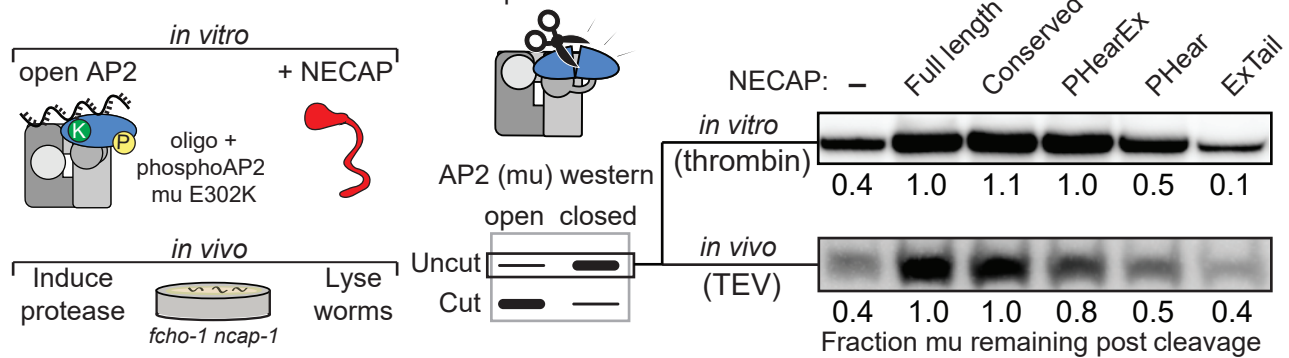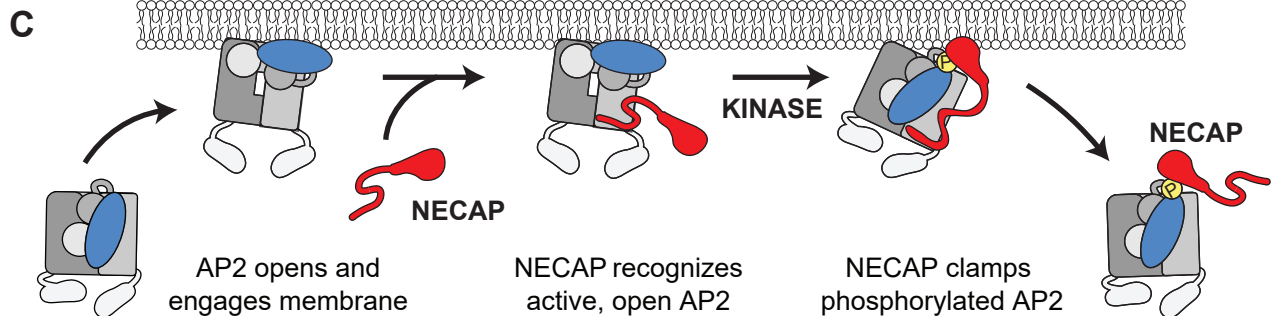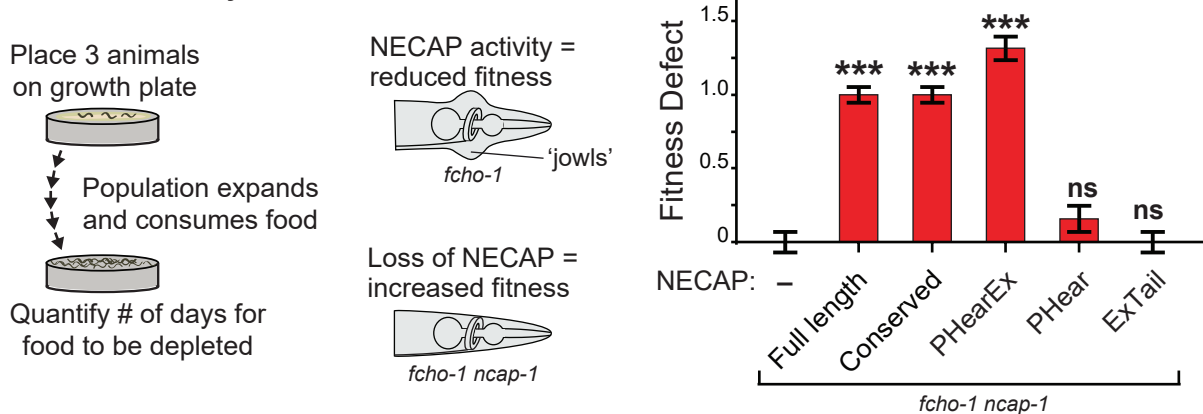# Figure 6. The AP2-NECAP$_{Ex}$ interface is required for inactivation.

Figure 7. NECAP clamps AP2 in a closed, inactive conformation.

A Protease sensitivity assays

B *In vivo* fitness assay

C

A 2D classification: 890,658 picks, 25 Å/pixel

1 μM   5 μM   5 μM + 0.05% β-OG

B 3D classification (1 class), re-center and re-extract
3D auto-refine: 490,560 particles

local CTF/
beamtilt
estimation

Masking and
signal subtraction

3.7 Å resolution   2.9 Å resolution

3D classification without alignment (K=6, T=8)

12.8%   16.3%   17.4%

14.6%   24.2%   14.7%

3D auto refine

71,571 particles
300 pixel box
1.16 Å/pixel

3.2 Å resolution

C

Local Resolution (Å)

3.1   3.3   3.6   3.9   4.2

D

Final resolution = 3.2 Ångstroms

GSFSC Masked
GSFSC Unmasked

0.143

Fourier Shell Correlation
Spatial Frequency (1/Å)

E

Histogram and Directional FSC Plot for pAP2NECAPjob156
Sphericity = 0.950 out of 1, Global resolution = 3.19 Å.

Histogram of Directional FSC
±1 S.D. from Mean of Directional FSC
Global FSC

Percentage of Per Angle FSC (%)
Directional Fourier Shell Correlation
Spatial Frequency (Å⁻¹)

F

% Residues
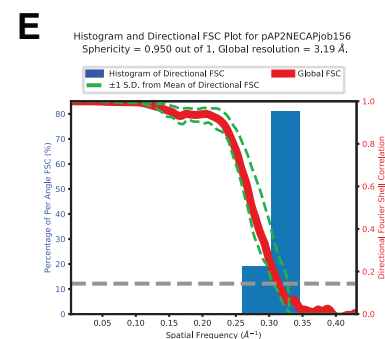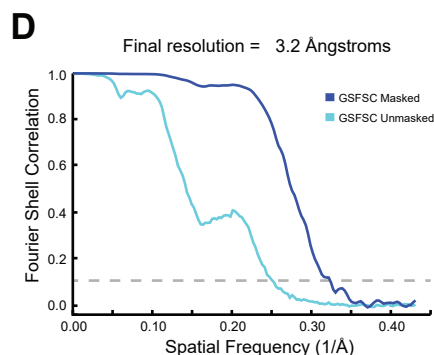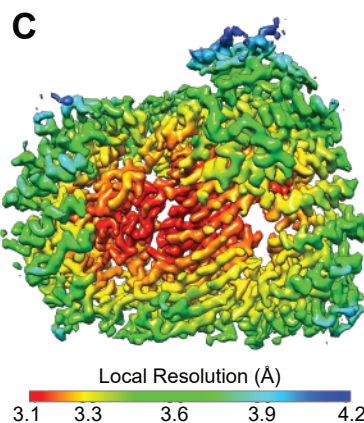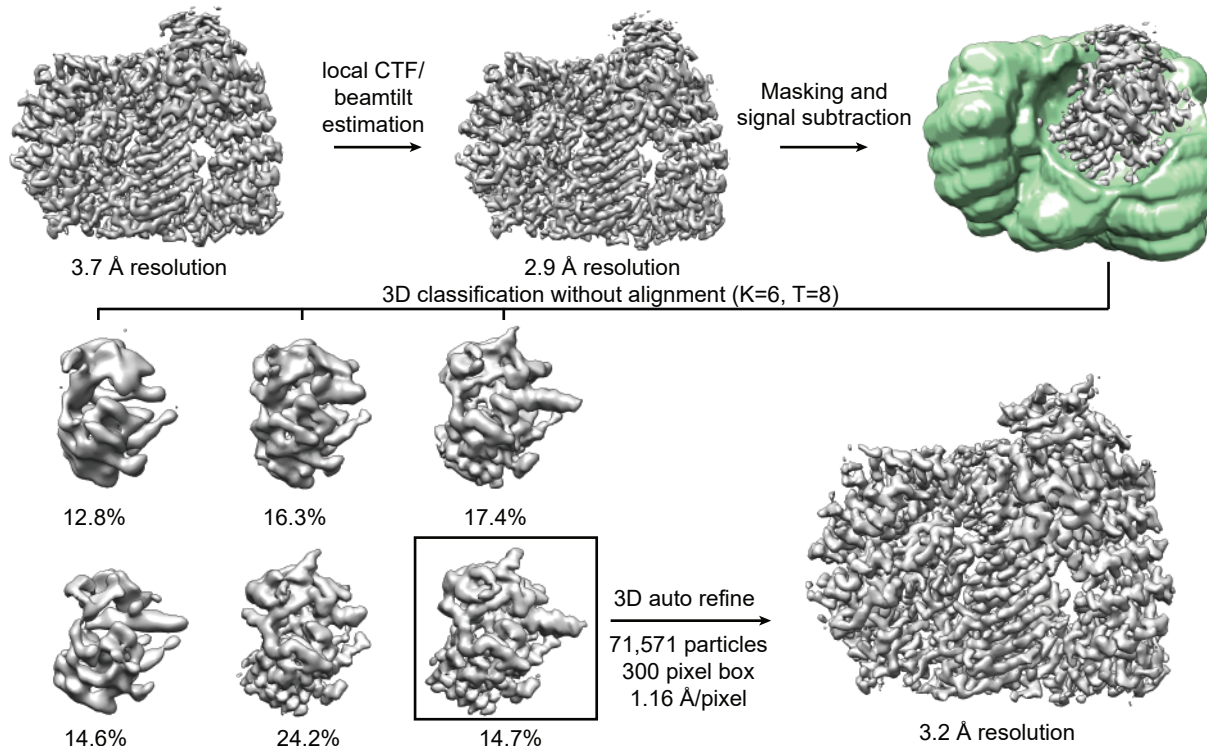Cα RMSD (Å)

Cα RMSD (Å)
0   2   4

Figure 1—figure supplement 1. Classification, signal subtraction, and refinement of phosphoAP2 bound to NECAP

A. Representative 2D class averages demonstrating different particle orientation preferences under different grid preparation conditions.
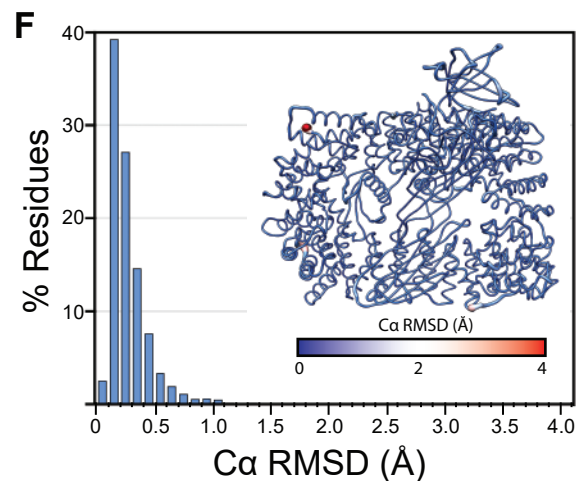
B. Processing workflow for 3D classification and refinement of phosphoAP2-NECAP using the Relion 3 software suite.

C. Cryo-EM map colored by local resolution (Relion 3).

D. Fourier Shell Correlation (FSC) plot

E. 3D FSC plot. An overall sphericity of 0.95 shows that resolution is nearly uniform in three dimensions.

F. Histogram plot of Cα RMSD of top ten molecular models from Rosetta refinement. Inset shows molecular model colored and scaled by RMSD.
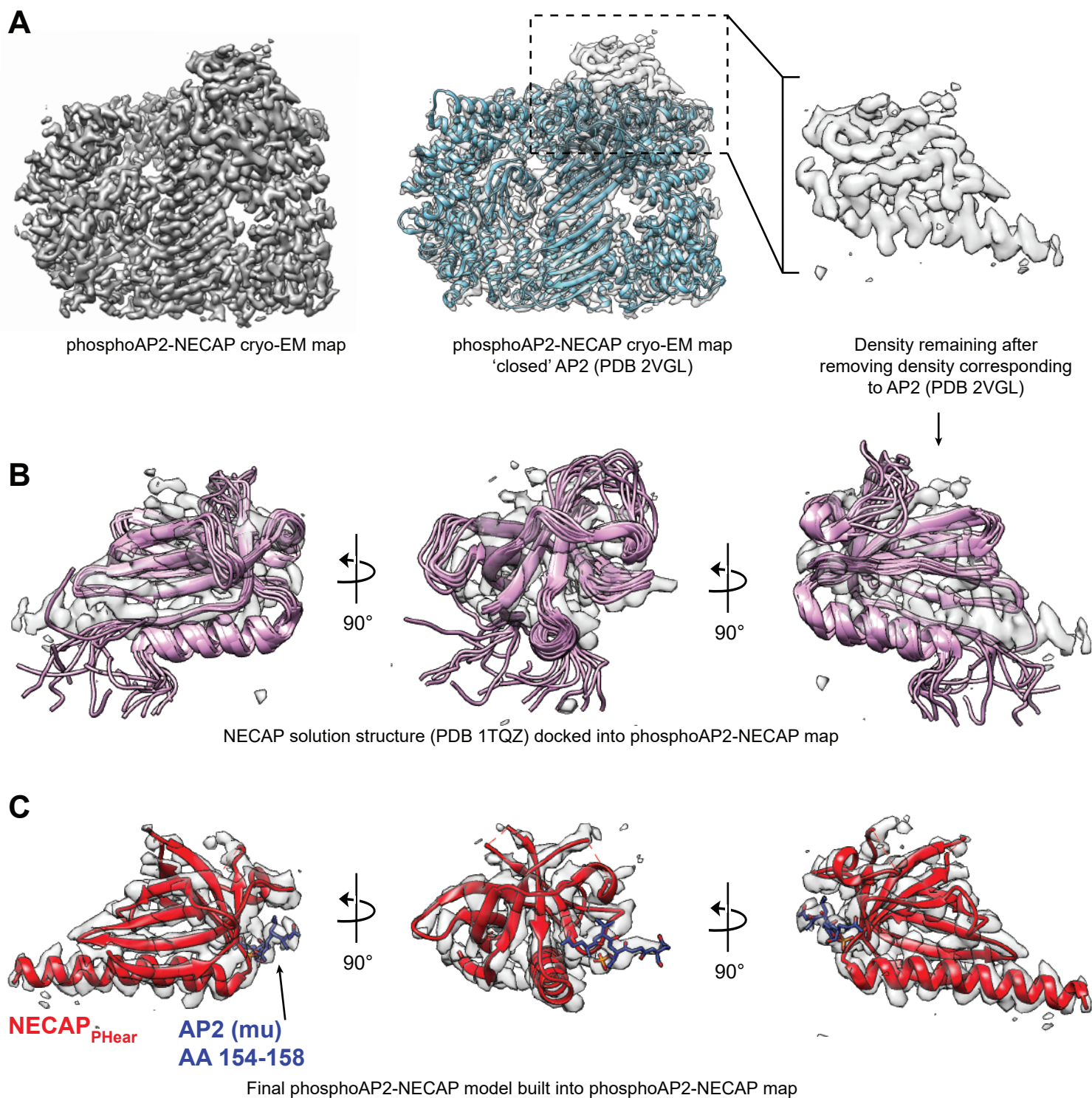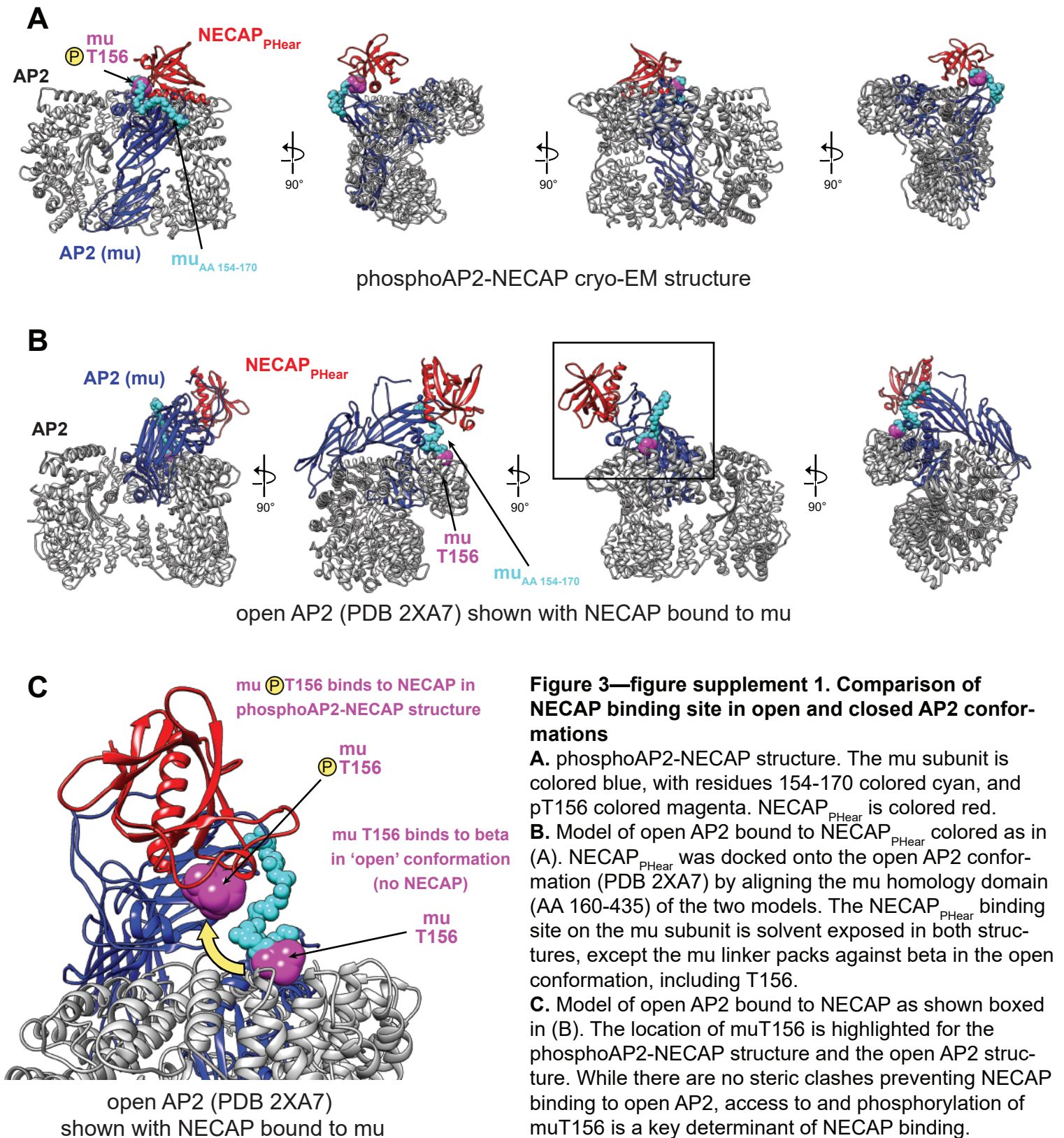
A. phosphoAP2-NECAP cryo-EM map

phosphoAP2-NECAP cryo-EM map 'closed' AP2 (PDB 2VGL)

Density remaining after removing density corresponding to AP2 (PDB 2VGL)

B. NECAP solution structure (PDB 1TQZ) docked into phosphoAP2-NECAP map

C. NECAP$_{PHear}$ AP2 (mu) AA 154-158

Final phosphoAP2-NECAP model built into phosphoAP2-NECAP map

Figure 1—figure supplement 2. Comparison of NECAP solution structure and phosphoAP2-NECAP cryo-EM structure

A. Cryo-EM map of phosphoAP2-NECAP is shown with a solid surface (left) and with a transparent surface with the closed AP2 crystal structure docked (middle). Masking the region corresponding to AP2 and subtracting this density from the full map gives a psuedo difference density map (right).

B. Solution structure of NECAP$_{PHear}$ (PDB 1TQZ) docked into the difference density from (A). NECAP$_{PHear}$ comprises a single alpha helix and beta sheet, which can be clearly seen in the cryo-EM density. However, the solution structure has some conformational differences compared to the AP2-bound cryo-EM structure.

C. The molecular model for NECAP$_{PHear}$ and AP2 mu (AA 154-158) are shown in the cryo-EM density. PDB 1TQZ was used as a starting model to manually rebuild in Coot and refine using Rosetta.
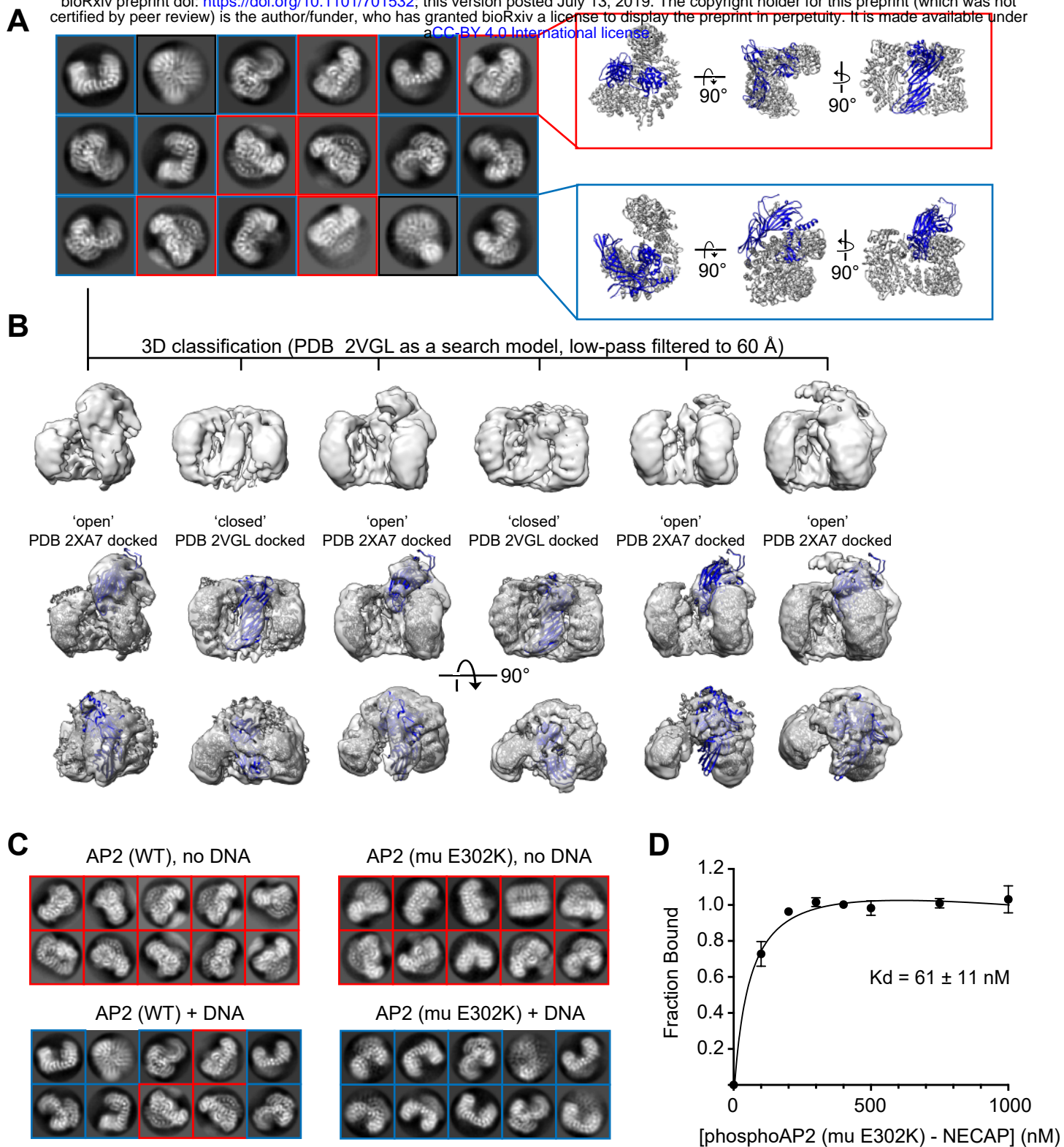
A phosphoAP2-NECAP cryo-EM structure

B open AP2 (PDB 2XA7) shown with NECAP bound to mu

C open AP2 (PDB 2XA7) shown with NECAP bound to mu

Figure 3—figure supplement 1. Comparison of NECAP binding site in open and closed AP2 conformations

A. phosphoAP2-NECAP structure. The mu subunit is colored blue, with residues 154-170 colored cyan, and pT156 colored magenta. NECAP$_{PHear}$ is colored red.

B. Model of open AP2 bound to NECAP$_{PHear}$ colored as in (A). NECAP$_{PHear}$ was docked onto the open AP2 conformation (PDB 2XA7) by aligning the mu homology domain (AA 160-435) of the two models. The NECAP$_{PHear}$ binding site on the mu subunit is solvent exposed in both structures, except the mu linker packs against beta in the open conformation, including T156.

C. Model of open AP2 bound to NECAP as shown boxed in (B). The location of muT156 is highlighted for the phosphoAP2-NECAP structure and the open AP2 structure. While there are no steric clashes preventing NECAP binding to open AP2, access to and phosphorylation of muT156 is a key determinant of NECAP binding.

A

B

3D classification (PDB 2VGL as a search model, low-pass filtered to 60 Å)

C

AP2 (WT), no DNA   AP2 (mu E302K), no DNA

AP2 (WT)

D

Kd = 61 ± 11 nM

Fraction Bound

noAP2 (mu E302K) - NECAP] (nM)

Figure 4—figure ... of an anionic polymer (DNA).

A. 2D class averages for WT AP2 + DNA are shown. Averages corresponding to the closed conformation (red inset) and open conformation (blue inset) are shown next to their respective molecular models (PDB 2VGL; PDB 2XA7).

B. 3D classification shows that the dataset contains a mixture of open and closed conformations. Classification was performed in Relion 3. Resolution is limited for all open structures because of an extreme prefered orientation in the cryo-EM grids.

C. Representative 2D class averages from AP2 samples. Mutations and the presence of DNA are labeled. DNA is in a 5-fold molar excess. Closed 2D classes are boxed in red, open 2D classes are boxed in blue.

D. Binding curve of phosphoAP2(mu E302K)-NECAP and a 47 bp ssDNA oligo. 20 nM DNA was incubated with increasing amounts of phosphoAP2-NECAP. A native gel shift assay was used to measure binding. Data was plotted and analyzed using the Prism software package.
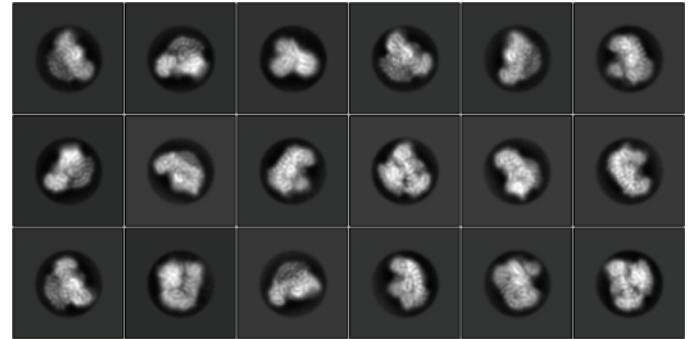
A Data collection: 1126 movies

5 μM AP2
25 μM ssDNA
+ 0.05% β-OG

100 nm
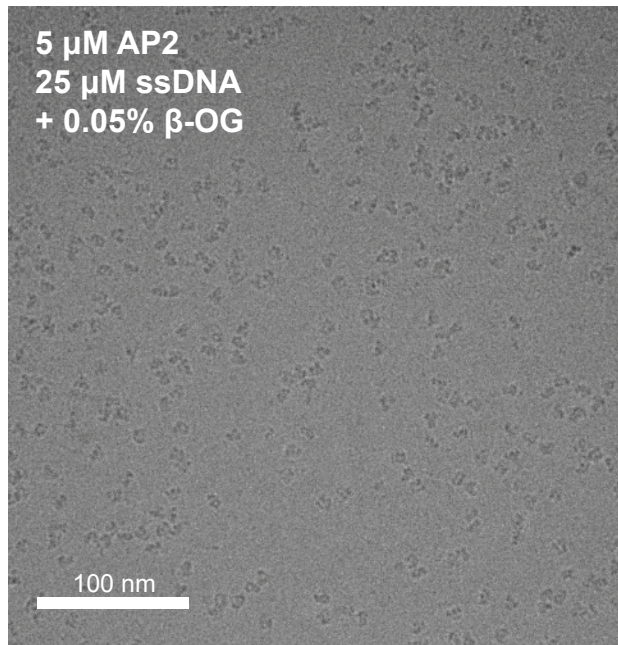
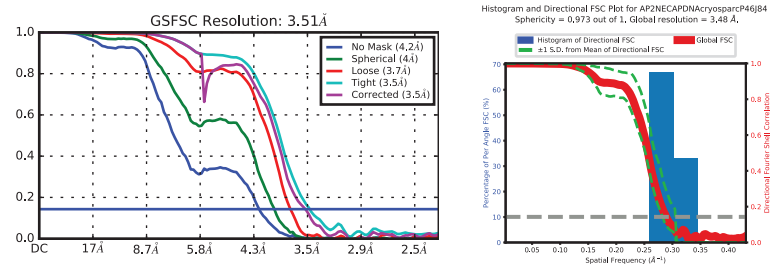**B** 2D classification: 717,231 particles (2.32 Å/ pixel)
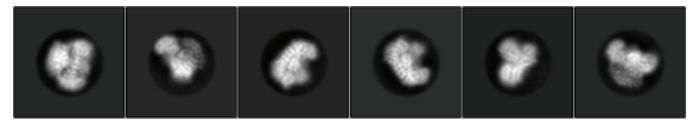
2D classification
Particle re-centering
388,995 particles (2.32 Å/ pixel)

ab initio model generation (cryoSPARC v2)
388,962 particles (1.16 Å/ pixel)

Non-Uniform refinement (cryoSPARC v2)
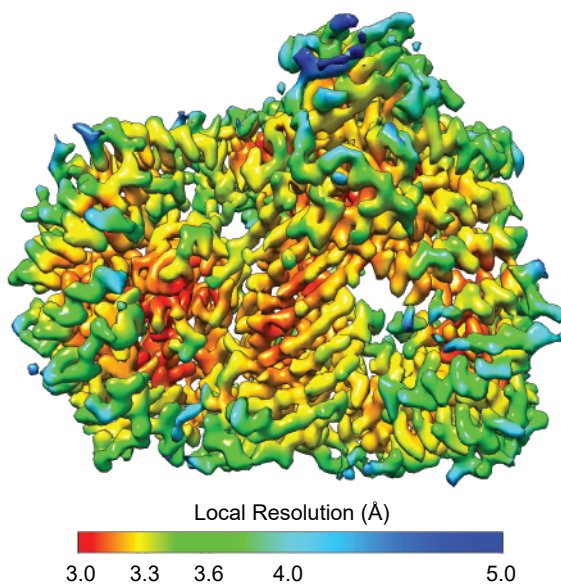324,922 particles (1.16 Å/ pixel)

C

Local Resolution (Å)

3.0   3.3   3.6   4.0   5.0

D

Figure 5—figure supplement 1. Cryo-EM data collection, processing, and model building for phosphoAP2-NECAP-DNA 'clamped' structure.
**A.** Representative motion-corrected, dose-weighted cryo-EM micrographs of phosphoAP2-NECAP-DNA complex.
B. Classification and refinement pipeline used for structure determination. Particles were extracted and 2D classified in Relion3. 'Clean' particles were re-extracted and used for *ab initio* model generation and refinement in cryoSPARC v2. 2D and 3D FSC plots are shown for the final model.
C. Final cryo-EM structure colored by local resolution.
D. Histogram plot of Cα RMSD of top ten molecular models from Rosetta refinement. Inset shows molecular model colored and scaled by RMSD.
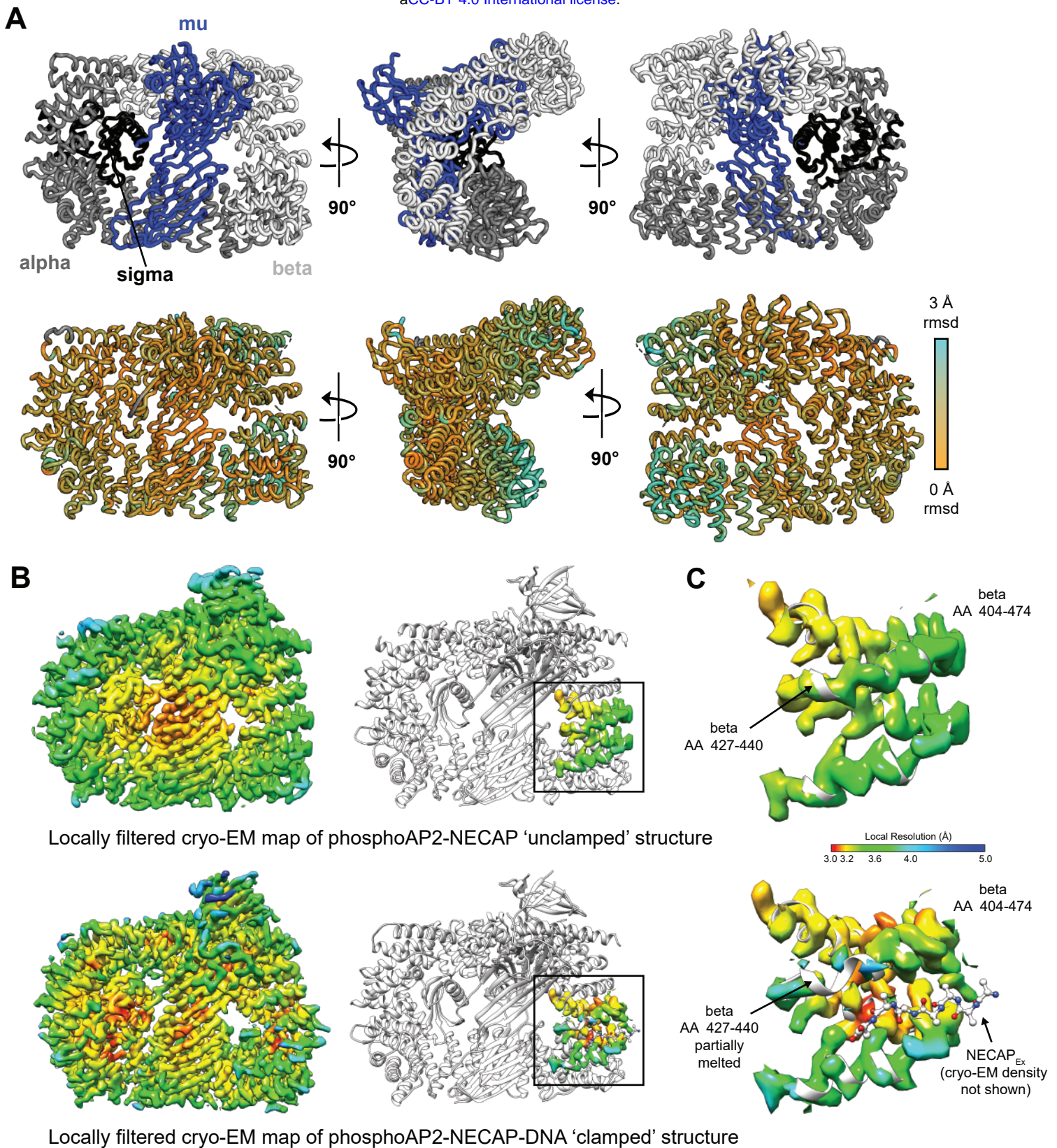
Locally filtered cryo-EM map of phosphoAP2-NECAP 'unclamped' structure

Locally filtered cryo-EM map of phosphoAP2-NECAP-DNA 'clamped' structure
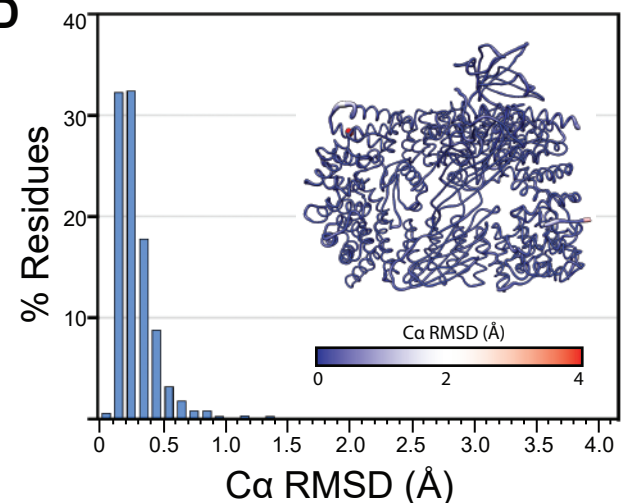
Figure 5—figure supplement 2. Structural comparison of 'unclamped' and 'clamped' phosphoAP2-NE-CAP structures

A. Cartoon diagram of phosphoAP2-NECAP 'unclamped' structure. NECAP is not shown.Top: AP2 subunits are colored as labeled. Bottom: AP2 is colored by per-residue RMSD. Values were calculated in PyMol using whole-molecule alignment of 'unclamped' vs 'clamped' phosphoAP2-NECAP.

B. Cryo-EM maps of 'unclamped' (top) and 'clamped' (bottom) phosphoAP2-NECAP structures. Maps were locally filtered by local resolution to standardize comparison between maps. Cryo-EM density corresponding to beta AA 404-474 is shown (right). Both maps are colored by local resolution using the same color gradient (color key in (C)).

C. The NECAP$_{Ex}$ binding site (beta AA 404-474) is shown for the 'unclamped' phosphoAP2-NECAP (top) and 'clamped' phosphoAP2-NECAP (bottom) structures. A small region of beta partially melts when the Ex domain is bound.
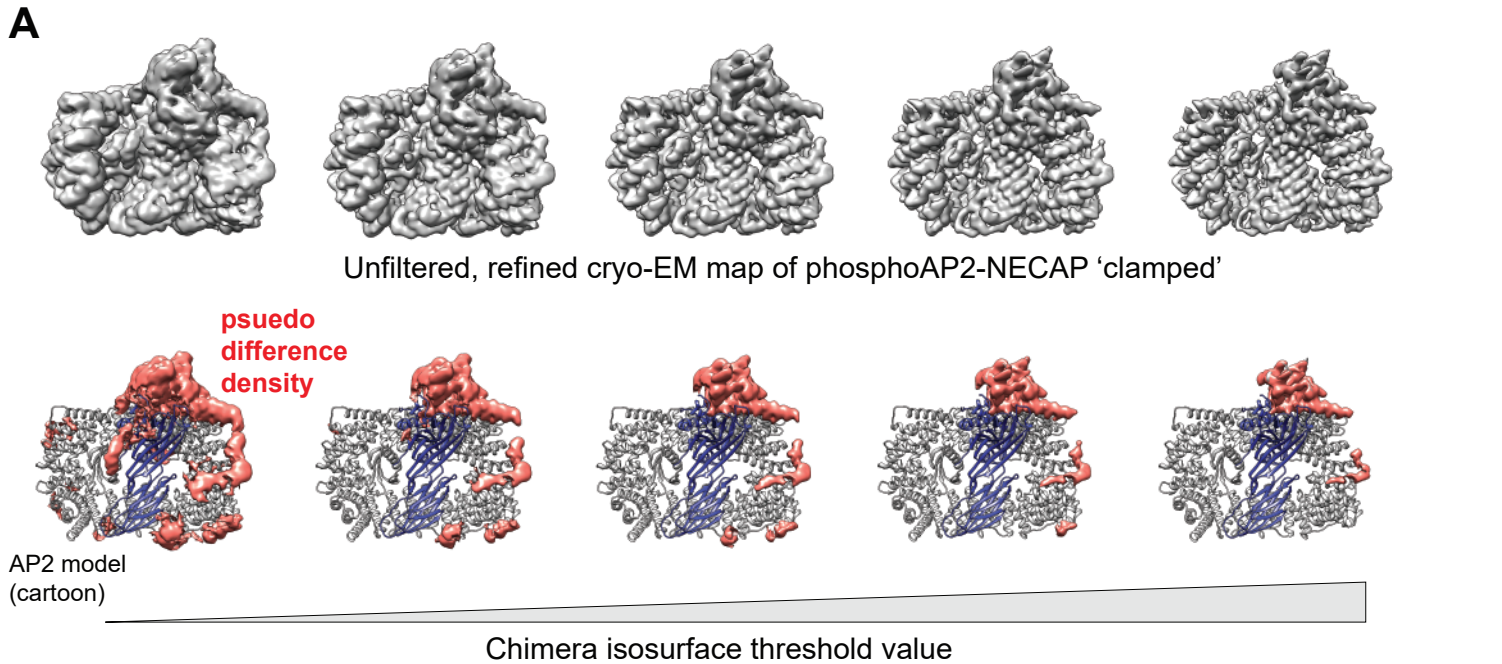
A

Unfiltered, refined cryo-EM map of phosphoAP2-NECAP 'clamped'

psuedo difference density

AP2 model (cartoon)

Chimera isosurface threshold value

Figure 6—figure supplement 1. The NECAP$_{Ex}$ domain binds along the surface of the beta subunit

A. The unfiltered, refined cryo-EM map of 'clamped' phosphoAP2-NECAP is shown at different isosurface threshold levels (top). A psuedo difference density map was made in Chimera by masking the region corresponding to AP2 and subtracting this map from the full map (bottom). The remaining density is shown colored salmon. The same threshold levels are shown top and bottom.

B. The psuedo difference density from (A) is shown at a low threshold level and with a Gaussian filter applied. Regions of the map corresponding to obvious AP2 features, such as loops omitted from our molecular model, were manually removed in Chimera. We hypothesize that a region of NECAP$_{Ex}$ cryo-EM density (boxed in red) corresponds to a conserved region of the sequence called the KEG motif (AA 153-154) . This is consistent with structural restraints based on the distance of this motif (16 residues) from the C-terminus of NECAP$_{PHear}$ in our molecular model (AA 8-137).

B

NECAP$_{PHear}$

NECAP$_{Ex}$

P$_S$LDLAF**KEG**QTI$_K$INI

129   163   236

PHear Ex Tail